Since January 2020 Elsevier has created a COVID-19 resource centre with free information in English and Mandarin on the novel coronavirus COVID-19. The COVID-19 resource centre is hosted on Elsevier Connect, the company's public news and information website.

International Journal of Biological Macromolecules 245 (2023) 125444

Contents lists available at ScienceDirect

International Journal of Biological Macromolecules

journal homepage: www.elsevier.com/locate/ijbiomac

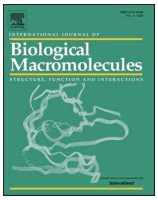

Targeting DPP4-RBD interactions by sitagliptin and linagliptin delivers a potential host-directed therapy against pan-SARS-CoV-2 infections

Shailendra Mani [a,1], Anupamjeet Kaur [b,1], Kamini Jakhar [a], Geetika Kumari [b], Sudipta Sonar [a], Amit Kumar [b], Sudesna Das [c], Santosh Kumar [b], Vijay Kumar [b], Rakesh Kundu [d], Anil Kumar Pandey [e], Umesh Prasad Singh [c], Tanmay Majumdar [b,*]

[a] Translational Health Science and Technology Institute, Faridabad, India
[b] National Institute of Immunology, New Delhi, India
[c] CSIR-Indian Institute of Chemical Biology, Kolkata, India
[d] Department of Zoology, Visva-Bharati University, Santiniketan, West Bengal, India
[e] Department of Physiology, ESIC Medical College & Hospital, Faridabad, India

ARTICLE INFO

Keywords:
Pan-SARS-COV-2
DPP4-RBD complex
ACE2-RBD interaction, repurposed therapy

ABSTRACT

Highly mutated SARS-CoV-2 is known aetiological factor for COVID-19. Here, we have demonstrated that the receptor binding domain (RBD) of the spike protein can interact with human dipeptidyl peptidase 4 (DPP4) to facilitate virus entry, in addition to the usual route of ACE2-RBD binding. Significant number of residues of RBD makes hydrogen bonds and hydrophobic interactions with α/β-hydrolase domain of DPP4. With this observation, we created a strategy to combat COVID-19 by circumventing the catalytic activity of DPP4 using its inhibitors. Sitagliptin, linagliptin or in combination disavowed RBD to establish a heterodimer complex with both DPP4 and ACE2 which is requisite strategy for virus entry into the cells. Both gliptins not only impede DPP4 activity, but also prevent ACE2-RBD interaction, crucial for virus growth. Sitagliptin, and linagliptin alone or in combination have avidity to impede the growth of pan-SARS-CoV-2 variants including original SARS-CoV-2, alpha, beta, delta, and kappa in a dose dependent manner. However, these drugs were unable to alter enzymatic activity of PLpro and Mpro. We conclude that viruses hijack DPP4 for cell invasion via RBD binding. Impeding RBD interaction with both DPP4 and ACE2 selectively by sitagliptin and linagliptin is an potential strategy for efficiently preventing viral replication.

1. Introduction

The RBD of the spike protein interacts with the ACE2 receptor [1,2], which is a recognised method of human-to-human transmission of the SARS-CoV-2 virus [3–5]. However, current paradox suggests that SARS-CoV-2 infection causes lymphopenia, where RNA and antigens are found in peripheral blood cells including lymphocytes (T, B, and NK cells) which do not express ACE2 or TMPRSS2 [6–8]. Even RBD can interact with a wide range of human cell types that lack ACE2 [6]. It implies that RBD can engage in interactions with host cells via alternative receptors other than ACE2. As an illustration, the major receptor for middle east respiratory syndrome coronavirus (MERS-CoV) is transmembrane protein, DPP4 (also known as CD26) [9–11]. It's noteworthy to mention that, in addition to the main receptor, several transmembrane proteins are usually necessary for virus entry into the target cell. It implies that the interaction between the RBD-spike and the human DPP4 is a crucial factor in aggravating the pathogenicity of SARS-CoV-2 [12–18]. A variety of epithelial, endothelial, and lymphocyte membranes express this plasma membrane glycoprotein [19,20]. For the treatment of type 2 diabetes (T2DM), it is regarded as a crucial therapeutic target. DPP4 inhibitors include sitagliptin, saxagliptin, vildagliptin, metformin, and linagliptin as examples of prospective therapies that could be investigated for COVID-19 treatment [21]. Several DPP4 inhibitors have shown conflicting results when used against SARS-CoV-2 [22]. Several genetic variants from the initial wild-type SARS-CoV-2 strain (Wt-SARS-CoV-2) have emerged throughout the pandemic since December 2019. Specific mutations within the Wt-RBD domain of Wt-SARS-CoV-2 culminate in the generation of various variants of concern (VOCs) defined by the

* Corresponding author.
E-mail address: majumdart@nii.ac.in (T. Majumdar).
[1] First author.

https://doi.org/10.1016/j.ijbiomac.2023.125444
Received 15 February 2023; Received in revised form 13 June 2023; Accepted 14 June 2023
Available online 27 June 2023

WHO [23,24]. The most common VOCs are like B.1.1.7 (α-variant, N501Y substitution), B.1.351 (β-variant, combination of K417N, E484K, and N501Y substitution), B.1.617.2 (δ-variant, combination of L452R and T478K substitution), and B.1.617.1 (κ-variant, combination of L452R/E484Q). The major protease (Mpro/3CLpro; nsp5) and the papain-like protease (PLpro; nsp3) of the viral cysteine proteases constitute significant targets for mitigating viral infection. The Mpro, a class of highly conserved cysteine hydrolases are able to cleave polyproteins at different locations and create multiple functional proteins throughout the course of virus multiplication. Viral multiplication also requires PLpro. Therefore, inhibiting these enzymes is a highly effective antiviral treatment strategy [25,26]. In this study, we established RBD can interact with DPP4 other than ACE2 for the viral entry. Our vision is to develop a therapeutic strategy that can prevent the entry of all variants by eliminating the interactions of RBD with both DPP4 and ACE2. In search of potent inhibitors, structure assisted drug design and cellular research with live pan-virus variants demonstrated that particular gliptin, alone or in combination, can suppress the growth of SARS-CoV-2 variants. This will accelerate the discovery of clinically efficient therapeutic strategies for curtailing SARS-CoV-2 infection.

2. Materials and methods

2.1. Ethics statement

We obtained ethical approval from the Institutional Bio-Safety Committee of National Institute of Immunology prior to conducting all studies: IBSC/448/2021 and IBKP-TAI No. C100833. The Institutional Bio-Safety Committee of THSTI also approved ethical permission for experiments involving live viruses: IBSC/200/2020, THS/298/2021 and IBKP-TAI No: C100458. All cellular experiments were carried out atleast three times independently in different cell lines.

2.2. Lineage of virus and its culture condition

B.6 lineage isolation of SARS-CoV-2 has been described earlier [28]. In this study, 5 variants of SARS-CoV-2 were used. The original Wt-SARS-CoV-2 isolate was designated as USA-WA1/2020, NR-52281, and its accession no is MN985325, GISAID: EPI_ISL_404895, GenBank: MT020880. The B.1.1.7 (α-variant) from the United Kingdom denoted as USA/CA_CDC_5574/2020, NR-54011, and genebank: GISAID is EPI_ISL_751801. South African origin B.1.351 (β-variant) isolate comprises of hCoV-19/South Africa/KRISPK005325/2020, NR-54009, and its gene accession no is GISAID: EPI_ISL_678615. The Indian origin B.1.617.2 (δ-variant) isolate is known as THSTI_287, and its gene accession no is GenBank: MZ356566.1 [29]. The USA origin B.1.617 (κ-variant) is named as USA/CA-Stanford-15_S02/2021, and its gene accession no is GenBank: GISAID: EPI_ISL_1675223. Vero E6 (CRL1586) and Calu-3 (HTB55) cell lines were cultured in Dulbecco's modified Eagle medium (DMEM; Lonza) supplemented with 10 % fetal bovine serum (FBS; Himedia), 100 U/ml of penicillin, 100 μg/ml of streptomycin. All SARS-CoV-2 variants were propagated in Vero E6 cells or Calu-3 cells and virus passaging was restricted to 4–8 passages only. All the virus stocks were authenticated by whole genome sequencing as described in earlier information [27,30].

2.3. Molecular docking analysis

Direct binding to DPP4 and entry into the targeted cells are both made possible by the RBD of the spike protein of the SARS-CoV-2 virus. In the present study, molecular docking was performed to identify critical interactions and binding sites of DPP4 with Wt-RBD of the SARS-CoV-2 virus. The Wt-RBD crystal structure (PDB: 6LZG, Sec. S1) [31] of the original SARS-CoV-2 will be used in our study. For our docking analysis with several variants, we have selected crystal structures of RBD from the Protein Data Bank (PDB), such as PDB:7EKF for B.1.1.7 (α-RBD) [32], PDB:7WCR for B.1.351 (β-RBD) [33], PDB:7W9F for B.1.617.2 (δ-RBD) [34] and PDB:7SOC for B.1.617 (k-RBD) [35]. The structure of human DPP4 (PDB:4L72, Sec. S1) was retrieved from PDB [36]. All the water molecules, metal ions, and other residues like NAG or SO4 were removed from the crystal structures for molecular docking analysis. The blind protein:protein docking simulations between the RBD of various variants with human DPP4 molecule was performed using ClusPro 2.0 [37]. During the docking calculation, all the default parameters were used. PyMol was used to find the interacting residues within the binding pocket of the DPP4:RBD docked complex [38]. The molecular interactions between protein-protein complexes including hydrogen bonds and the bond lengths were analysed and depicted by using Ligplot+2.2.5. software [39]. PRODIGY server with a default 25 °C temperature setting was used for the binding affinity calculations of docked complexes [40].

The 3D structures of FDA approved DPP4 inhibitors [41,42], sitagliptin (PubChem CID: 4369359), linagliptin (PubChem CID: 10096344), vildagliptin (PubChem CID: 6918537), saxagliptin (PubChem CID: 11243969) and metformin (PubChem CID: 4091) were downloaded from the PubChem database. The molecular docking was performed using AutoDock Vina software [43]. The dimension of the grid box was set to 84 × 94 × 118 $Å^3$ with grid centre at −14.658, −54.126, and −17.185 using ADT tools. In addition, the molecular interaction between ACE2-RBD complex (PDB: 6LZG, Sec. S1) [44] with gliptin (linagliptin and sitagliptin) was studied. All the water molecules, metal ions, and other residues were removed from the crystal structure of ACE2-RBD for docking analysis. The dimension of the grid box was set to 126 × 108 × 126 $Å^3$ with grid centre at −31.113, 18.322, and −6.901 using ADT tools. The docked poses of ligand were clustered at 0.2 nm tolerance for RMSD and ranked based on binding energy. Out of 9 poses obtained in AutoDockVina, the best pose which lies within the binding pocket of protein with low free binding energy (B.E.) was selected for further analysis.

2.4. Human DPP4 and ACE2 gene targeting

The DPP4 CRISPR/Cas9 KO plasmid (Santa Cruz, sc-400862) was transfected into Calu-3 cells to disrupt gene expression by causing a double-strand break (DSB) in a 5′ constitutive exon of the DPP4 (human) gene to create DPP4 knockout cells. Similarly, ACE2 CRISPR/Cas9 KO Plasmid (Santa Cruz, sc-401131-KO-2) was used to develop ACE2 knockout cells. The deletion of gene in Calu-3 cells was confirmed by immunoblotting (Fig. S1).

2.5. Microscopic study

ACE2 knockout and DPP4 knockout Calu-3 cells (2.0×10^5/well) were plated separately onto cover glasses in a 9 cm^2 well of the plates, grown overnight (to ~5×10^5 cells), and transfected with Wt-RBD-Fc-IgG1 (Addgene # 141183) construct using lipofectamine 3000 (Invitrogen) following manufacturer's instructions. 0.8 μg plasmid was used for transfection per 5×10^5 cells in each 4 cm^2 well of the plate. After 8 h post-transfection, cells were fixed in formaldehyde for 5 min and permeabilized with PBS containing 0.1 % Triton X-100. Fixed cells were blocked in PBS containing 1 % BSA for 1 h. Afterward, cells were incubated with either a primary antibody specific to DPP4 or ACE2 (Abcam, ab15348) or an anti-IgG1-Fc-AF488-labelled antibody (Invitrogen, A10631), followed by an alexa-fluor 647 tagged anti-rabbit secondary antibody (Abcam, ab150079) specific to primary antibody of DPP4 or ACE2. Mounting was done using fluoroshield (Sigma), and cells were visualized under a confocal laser scanning inverted microscope, Carl-Zeiss LSM980 (63×)2.

2.6. Immunoprecipitation, and immunoblot

Calu-3 cells (2.0×10^5/well) were plated onto cover glasses in 9 cm^2

well of the plates, grown overnight (to ~5 × 10^5 cells), and was transfected with pLEX307-DPP4-puro (Addgene # 158451) alone or in combination with pCDNA3.1-RBD construct using lipofectamine 3000 (Invitrogen) following manufacturer's instructions. DPP4 knockout cells were utilised in one set to transfect the pCDNA3.1-RBD construct in order to perform the DPP4-RBD immunoprecipitation assay, which would verify the absence of any experimental artefact. In a separate experiment, pcEP4-myc-ACE2 was transfected with pCDNA3.1-RBD construct. 0.8 μg plasmid was used for transfection per 5 × 10^5 cells in each 4 cm^2 well of the plate. After 8 h post-transfection, cells were treated with sitagliptin or linagliptin or their combination for 24 h. Then cells were lysed in lysis buffer containing 20 mM HEPES (pH 7.4), 50 mM NaCl, 1.5 mM $MgCl_2$, 2 mM DTT, 2 mM EGTA, 10 mM NaF, 12.5 mM β-glycerophosphate, 1 mM Na_3VO_4, 5 mM $Na_4P_2O_7$, 0.2 % (v/v) Triton X-100, and protease inhibitors (Himedia). Cellular lysates, containing 400 μg of total protein were precleared with mouse immunoglobulin G (IgG) agarose (Sigma) in IP buffer for 1 h, and then incubated overnight with IP-specific DPP4 antibody (cell signalling, 67,138), or myc-specific antibody and then with protein A/G beads for 1 h with rotation. After incubation, the beads were washed with 1× PBS, and protein complexes were eluted by adding 40 μl of 2× sample buffer to each IP reaction and heating at 50 °C for 15 min. For immunoblot, cells were lysed in the 1.5× Laemmli sample buffer containing protease inhibitor cocktails (Himedia) and for phospho-antibody, phosphatase inhibitor cocktails (Cell Signalling Technology) were additionally used. After sonication, samples were heated at 95 °C and equal amounts of proteins were analysed on denaturing SDS-polyacrylamide gels after estimation of protein. The proteins were transferred to the PVDF blotting membrane (Amersham Hybond) and probed with primary-antibody specific for RBD (Abcam, ab283946), DPP4, and ACE2 individually. Secondary antibody conjugated to horseradish peroxidase (HRP) were then used and bands were visualized by a chemiluminescence-based detection system (Amersham) using SuperSignal West Femto/Pico Plus substrate (Thermo-Fischer Scientific). β-actin was used as a control for normalization [45].

2.7. Molecular dynamics (MD) simulation studies

In the current investigation, 9 systems were established for MD simulation. The nine systems that were tested for 100 ns each were DPP4, DPP4 + linagliptin, DPP4 + sitagliptin, WtRBD-DPP4, WtRBD-DPP4 + linagliptin, WtRBD-DPP4 + sitagliptin, WtRBD-ACE2, WtRBD-ACE2 + sitagliptin, and WtRBD-ACE2 + linagliptin. All the simulations were carried out using a GROMACS-2022 software package [46]. The protein alone and protein-ligand complex were solvated in a cubic box using simple point charge (SPC) water molecules. The additional (0.15 M NaCl) Na and Cl ions were used to neutralize the system. The force field parameters for the ligands were obtained from the Automated Topology Builder (ATB) [47]. The CHARMM27 force field was used to generate the topology of all protein systems in explicit solvent [48]. We have performed 50,000 steps for the steepest descent energy minimization of all systems. A Verlet cutoff scheme was used with long-range electrostatics calculated by the particle-mesh Ewald (PME) method [49]. The pressure and temperature were kept at 1.0 bar and 310 K using the Parrinello−Rahman barostat [50] and modified Berendsen thermostat [51], respectively, for the MD simulation. Lincs constraint algorithm was used for constraining the atoms. The graphs were generated using OriginPro 9.0 software and molecular structures were visualized by PyMOL software. The MD trajectories were analysed using GROMACS tools. The conformational stability of proteins in the absence or presence of ligands was analysed using gmx rms, gmx rmsf, gmx gyrate and gmx sasa tools.

2.8. Calculation of binding free energy ($\Delta G_{binding}$) of gliptins

Poisson–Boltzmann surface area (MM–PBSA) approach of the molecular mechanics was used to calculate the $\Delta G_{binding}$ between protein-ligand systems [52]. The $\Delta G_{binding}$ was evaluated for the following systems: (i) WtRBD-DPP4 with linagliptin, (ii) WtRBD-DPP4 with sitagliptin, (iii) WtRBD-ACE2 + linagliptin, (iv) WtRBD-ACE2 + sitagliptin using g_mmpbsa tool. The impact of conformational entropy was ignored while calculating the relative binding free energy because of its small impact on the total binding free energy and high computational expense. The B.E. was calculated as the average over the last 300 frames in the aforementioned MD simulation systems.

2.9. Cells viability assay

Only cells and virus infected cells were seeded in 96-well plates (10,000 cells/well in 150 μl medium) and treated with several gliptins, and remdesivir. Cells were analysed for proliferation by a colorimetric method for determining the number of viable cells, using the CellTiter 96® Aqueous One Solution Cell Proliferation Assay (Promega) as recommended by the manufacturer. The absorbance values were recorded at 490 nm after incubation at 37 °C for 4 h and corrected by subtracting the background absorbance (culture media alone). All samples were run twice in triplicate. Cell viability percentages were calculated as follows: cell viability % = [absorbance of treated cultures/absorbance of control cultures] × 100.

2.10. Determination of the efficacy of gliptins in limiting SARS-CoV-2 variants infection in vitro

Vero E6 cells were cultured overnight in 48-well plates, infected them with 400 TCID 50/well (200 ul/well) of each SARS-CoV-2 variant, and then incubated for 1 h at 37 °C CO_2 incubators with intermittent shaking. Then cells were washed with DMEM (without FBS) and then 500 μl of DMEM supplemented with 2 % FBS was added to each of the wells. The plates were incubated for 48 h at 37 °C CO_2 incubator in presence or absence of remdesivir and gliptins at different concentrations. Remdesivir was also used as a standard antiviral compound against SARS-CoV-2 infection [53]. The supernatant was collected at 48 h post-infection and qPCR was done to do absolute quantification of viral RNA copies using primers of nucleocapsid gene of SARS-CoV-2 based on CDC guidelines [53,54]. Two different set of primers (N1, and N2) of nucleocapsid gene were used and the absolute quantification of each gene was done to determine viral copy numbers/ml. For this, synthetic single stranded RNA with known copy number (Merck, EURM019) was used as a reference to generate the standard curve, with each run. All the experiments were done in triplicates with six biological repeats. Only cells and cells infected with various SARS-CoV-2 variants were kept to compare how much gliptins inhibited viral growth. Changes among treatment groups of cells or between sets of experiments were analysed by one-way ANOVA and Students *t*-test. Results were expressed as mean of virus log copy numbers/ml ± SD (standard deviation bars in graphs) of viral RNA copies, and presented in the log10 scale. *p*-values <0.01; and < 0.001 were considered statistically significant. Statistical analyses and data visualization were performed with the GraphPad Prism software Version 9.4.1(458).

2.11. DPP4 activity

Only cells, DPP4 KO cells, virally infected cells, or infected cells treated with gliptins were tested for the presence of enzymatically active DPP4 using DPP4-GloTM Protease Assay (G8350,Promega). Luminescence was recorded as relative light units (RLU) on a Dynex MLX luminometer 30 min after adding the DPPIV-Glo™ Reagent.

2.12. PLpro expression and purification

pK27Sumo_His-SUMO-PLpro (nsp3) (SARS-CoV-2) was a gift from John Diffley (Addgene plasmid # 169193; http://n2t.net/addgene

:169193; RRID:Addgene_169193) [55]. This construct was expressed in *Escherichia coli* BL21. The induction for expression was done at O·D 0.8 with 0.5 mM IPTG and incubated at 18 °C overnight. The cell pellet was lysed by sonication in a lysis buffer (50 mM Tris-HCl, pH 7.5, 10 % glycerol, 1 mM DTT, 0.02 % Triton X-100, 500 mM NaCl, and 30 mM imidazole). Before lysis, the cell suspension was incubated with 100 μg/ml lysozyme for 20 min and finally sonicated 25 times for 30s each with an off period of 30 s in between. The lysate was centrifuged to collect the supernatant from it. The His-SUMO-tagged PL-pro was purified by affinity chromatography using Ni-NTA. The supernatant was loaded in a pre-equilibrated Ni-NTA purification column (Column volume (cv) of 3 ml). The column was equilibrated with fresh lysis buffer (10 cv) and washed with the same buffer (20 cv). The protein was eluted with an elution buffer containing 50 mM Tris-HCl, pH 7.5, 10 % glycerol, 1 mM DTT, 0.02 % Triton X-100, 500 mM NaCl, and 400 mM imidazole. Eluted protein was dialyzed using a buffer containing 50 mM Tris-HCl, pH 7.5, 10 % glycerol, 1 mM DTT, 0.02 % TritonX-100 and 50 mM NaCl to reduce the salt and imidazole. The His-SUMO tag was cleaved with 0.02 mg/ml His-Ulp1. The cleaved protein was further purified using a Ni-NTA column to remove the His-SUMO tag and His-Ulp1. The protein was further purified using size-exclusion chromatography. The protein was loaded in a pre-equilibrated Sephacryl S-100 HR-16/60 column (Cytiva). The column was equilibrated with a buffer containing 25 mM HEPES-KOH, pH 7.6, 10 % glycerol, 0.02 % Triton X-100, 150 mM NaCl, and 2 mM DTT. The peak fractions, of 1 ml each, were collected and stored at 4 °C for PLpro inhibition assay.

2.13. Ulp1 expression and purification

pFGET19_Ulp1 was a gift from Hideo Iwai (Addgene plasmid # 64697; http://n2t.net/addgene:64697; RRID:Addgene_64697) [56]. The construct was expressed in *E. coli* BL21. The induction for expression was done at O·D 0.8 with 1 mM IPTG and incubated at 37 °C for 4 h. The cell pellet was lysed with a lysis buffer (50 mM Tris-HCl, pH 8, 5 mM magnesium acetate, 10 % glycerol, 1 mM DTT, 0.02 % Triton X-100, 500 mM NaCl, 20 mM imidazole). Before sonication-lysis, the cell suspension was incubated with 100 μg/ml lysozyme for 20 min and finally sonicated 25 times for 30 S each with 30 S off time in between. The cell lysate was centrifuged to collect the supernatant from it. The supernatant was loaded in a pre-equilibrated Ni-NTA purification column (cv - 3 ml). Ni-NTA was equilibrated with fresh lysis buffer (10 cv) and washed with the same buffer (20 cv). Finally, the protein was eluted with an elution buffer containing 250 mM imidazole (50 mM Tris-HCl, pH 8, 5 mM magnesium acetate, 10 % glycerol, 1 mM DTT, 0.02 % Triton X-100, 500 mM NaCl, 250 mM imidazole). In the final step of purification, the protein was loaded in a pre-equilibrated Sephacryl S-100 HR-16/60 column for size-exclusion chromatography. Before loading the protein on the column, the column was pre-equilibrated with the buffer (50 mM Tris-HCl, pH 8, 5 mM magnesium acetate, 10 % glycerol, 0.5 mM TCEP, 0.01 % Triton X-100, 500 mM NaCl). The eluted protein's peak fractions, each of 1 ml, were collected and stored at 4 °C for using it for the His-SUMO tag cleavage of PLpro.

2.14. Expression and purification of substrate for PLpro gel-based assay

pGEX4T1_GST-PLproCS-MBP was a gift from John Diffley (Addgene plasmid # 169195; http://n2t.net/addgene:169195; RRID: Addgene_169195) [55]. PLpro gel-based assay substrate (GST-PLproCS-MBP) was constructed such as it has a GST tag at the N terminus, MBP tag at the C terminus, and in between the two tags there is a PLpro recognition site or cleavage site (TLKGG//APTKV) (nsp2/3 junction). PLpro is expected to cleave this substrate at G//A which leads to two fragments (25 kDa, 42 kDa). The expression induction was done at O·D 0.8 with 1 mM IPTG at 37 °C for 4 h. The cell pellet was lysed with buffer (50 mM Tris-HCl, pH 7.5, 10 % glycerol, 1 mM DTT, 0.02 % Triton X-100, 300 mM NaCl). Before sonication-lysis, the cell suspension was incubated with 100 μg/ml lysozyme for 20 min and finally sonicated 25 times for 30 s with an off time of 30 s in between. The lysate was centrifuged to collect the supernatant from it. The supernatant was loaded in a pre-equilibrated GST purification column (cv-3 ml). GST was equilibrated with fresh lysis buffer (10 cv), and the supernatant was incubated with GST beads for 3 h at 4 °C and washed with the same buffer (20 cv). Finally, the protein was eluted with additional 50 mM reduced Glutathione containing lysis buffer. In the final step of purification, the protein was loaded in a pre-equilibrated Sephacryl S-100 HR-16/60 column for size-exclusion chromatography. The column was run with elution with buffer containing 25 mM HEPES-KOH, pH 7.6, 10 % glycerol, 0.02 % Triton X-100, 150 mM NaCl, and 2 mM DTT. The peak fractions were collected and stored at 4 °C for using it in PLpro Gel-based assay.

2.15. PLpro gel-based assay with Sitagliptin and linagliptin

5 μM of the enzyme (PLpro) was incubated with sitagliptin and linagliptin (each at 10 μM, 100 μM, and 500 μM concentrations) for 10 or 20 min (in case of 500 μM concentration of inhibitors). Then 5 μM of gel-based assay substrate GST-PLproCS-MBP was added to the pre-incubated enzyme with compounds. The whole reaction was done at RT (25 °C) for 5 h. The assay was done in buffer containing 50 mM HEPES-KOH, pH 8, 5 mM magnesium acetate, 10 % glycerol, 0.5 mM TCEP, 0.01 % Triton X-100 and 500 mM NaCl. The reaction products were visualized through 12 % SDS-PAGE gel, which was stained with Coomassie brilliant blue stain (VWR Life Sciences). Image-based densitometric analysis was done using ImageLab software (6.1 version).

2.16. Expression and purification of Mpro of SARS-CoV-2

Expression and purification of the Mpro protein was done according to the method described by Iketani, S., et al., 2022 [57].

2.17. Protease inhibition assay

The followed assay protocol was similar to protocol mentioned by Zhang et al. 2020 with slight modifications in it [58]. The protease inhibition assay was carried out using Dabcyl-KTSAVLQ↓SGFRKM-E (Edans)-NH2 fluorescent peptide substrate at 15 μM concentration. The inhibitors at 100 μM concentrations were incubated with 180 nM of protein for 20 min at room temperature. Total reaction volume was 50 μM. The reaction was initiated by adding 15 μM of substrate. Reactions were done in duplicate. Fluoroscence intensity observed by excitation at 340 nm and emission at 460 nm. Relative Fluorescence Unit (RFU) was measured at 20 min (due to better signal to noise ratio). Buffer used in assay consist of 20 mM Tris, 100 mM NaCl, 1 mM EDTA, 1 mM DTT, pH 7.3. For positive control Mpro-13b inhibitor has been used at 1 μM and 5 μM concentration while in case of negative control no inhibitor has been used. Inhibition assay has been done at final 5 % DMSO in reaction.

3. Results and discussions

3.1. Binding prediction of human DPP4 with Wt-RBD of SARS-CoV-2 spike protein

Experimental and computational studies have been performed to determine whether the Wt-RBD domain could interact with DPP4. Therefore, a blind molecular docking study was carried out again using the original crystallographic structure of the Wt-RBD domain of SARS-CoV-2 with human DPP4 protein (Fig. 1a; Fig. S2). In the best-docked position, Wt-RBD could interact with DPP4 with the favourable B.E. = −14.9 kcal/mol and dissociation constant (Kd) of 1.10E-11 M (Table 1). Five residues (L517, A520, G381, R357 and R355) of Wt-RBD domain form six hydrogen bonds with five residues (T736, T746, Q731, D243 and E244) present in the α/β-hydrolase domain of DPP4 (Fig. 1a). One salt-bridge was formed between the D243 (C=O) residue of DPP4

and R357 (NH2) of Wt-RBD. Significant number of residues of both Wt-RBD (17 amino acids from Y380-Y396, D428, T436, H519-A520 domain) and DPP4 (18 amino acids from F240-S242, F713-H754 domain) were involved in hydrophobic interactions, displayed the strong interaction between Wt-RBD and DPP4 (Fig. 1a and Fig. S2a; Table 1). Overall, hydrogen bonding and hydrophobic contacts were the major intermolecular forces that contribute to the favourable binding between Wt-RBD and DPP4 complex.

3.2. MD simulation of DPP4 and Wt-RBD complex

Further, we have performed the classical MD simulation to investigate the dynamic behaviour of Wt-RBD and DPP4 binding in an explicit solvent. According to the representative conformation of MD simulation of WtRBD-DPP4 complex, RBD interacted with the C-terminus region (721–754) of the α/β-hydrolase domain and D244 residue of the β-propeller domain of DPP4 (Fig. 1b). Intriguingly, RBD failed to engage with the adenosine deaminase (ADA) and fibronectin binding site of DPP4. It suggested that RBD didn't impede the DPP4's other essential catalytic function. According to the results of molecular docking, the LigPlot depiction of the intermolecular hydrogen bonds and hydrophobic interactions were the main interaction involved in the binding of RBD and DPP4 (Fig. 1c). The RBD-DPP4 complex movie amply demonstrated that Wt-RBD remained bound to the DPP4 during the simulation (Movie S1). Majorly, Q731, T746, D737 and E244 of DPP4 showed hydrogen bonding with L517, H519 and R357 of Wt-RBD during the simulation. According to the aforementioned findings, DPP4 could be a promising receptor for SARS-CoV-2 entry in host cells through its robust interaction with RBD.

3.3. Cell-surface binding of RBD to DPP4

To elucidate the interaction between the Wt-RBD and DPP4, we performed a cell-surface-binding assay using ACE2 knockout cells. Transfected RBD-Fc was detected by anti-IgG1-Fc-AF488-labelled antibody. The RBD-Fc was fused with alexa-fluor 647 labelled-secondary antibody specific to human DPP4 in ACE2 knockout cells. Confocal microscopic images subsequently showed that both RBD-Fc and DPP4

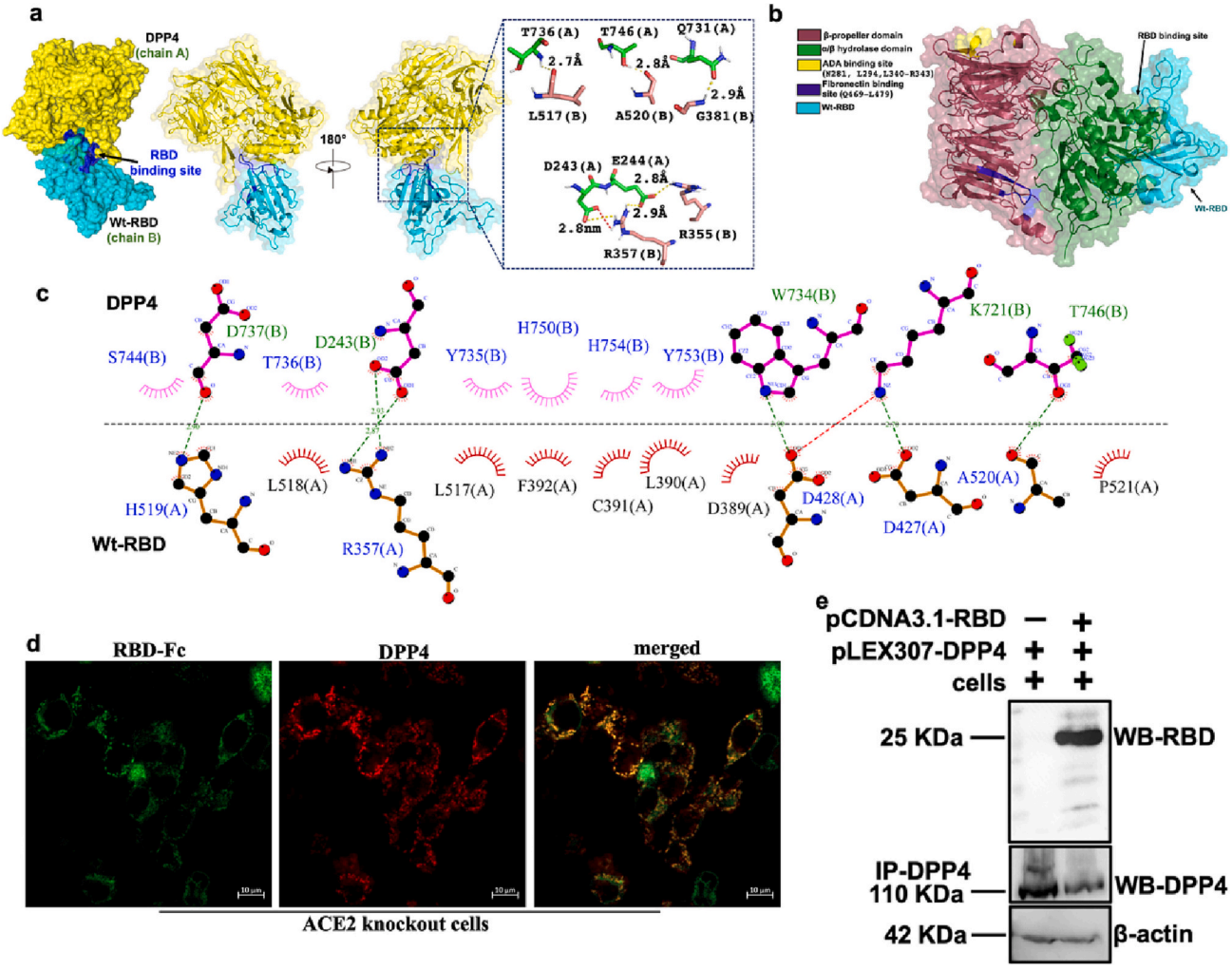

Fig. 1. Binding affinity of RBD with DPP4. a, The original crystallographic structure of the RBD domain (333–527 aa) of SARS-CoV-2 with human DPP4 protein (39–766 aa) was used for blind molecular docking. 'A' depicted residues of DPP4 and 'B' represented RBD residues. Hydrogen bonds were shown in yellow dotted lines, red dotted line represented salt bridge. b, Most populated conformation of MD simulation of Wt-RBD with DPP4 in which RBD interacted with the both C-terminus region (721–754) of the α/β hydrolase domain and D244 residue of the β-propeller domain of DPP4. c, 2D representation of most populated conformation of Wt-RBD-DPP4 simulation. The intermolecular hydrophobic contacts were shown in semi-circles, and hydrogen bonds were shown in green dashed lines. d, Representative confocal image of RBD-Fc (green) in ACE2 knockout cells stained with alexa-fluor 488 labelled-secondary antibody specific to IgG1-Fc and alexa-fluor 647 labelled-secondary antibody specific to DPP4 (red). Scale bar = 10 μm. e, Calu-3 cells were transfected with DPP4 expressing pLEX307-DPP4 alone or together with pCDNA3.1-RBD and both samples were immunoprecipitated with DPP4 antibody, and immunoblotted with RBD antibody. β-actin was used as an internal control. (For interpretation of the references to colour in this figure legend, the reader is referred to the web version of this article.)

Table 1
Molecular docking analysis of DPP4 with RBD variants of SARS-CoV-2 Spike protein.

Protein complex	Binding affinity ΔG (kcal/mol)	Dissociation constant Kd (M) at 25.0 °C	Residue involved in intermolecular hydrogen bonding		Residues involved in intermolecular hydrophobic contacts	
			RBD domain (T333-P576)	DPP4 (S39-P766)	RBD domain (T333-P576)	DPP4 (S39-P766)
WtRBD+DPP4	−14.9	1.10E-11	L517, A520, G381, R357, R355	T736, T746, Q731, D243, E244	A520, P521, A522, H519, L518, E516, C391, F392, L390, D427, L387, V382, Y380, D428, T430, F429, Y396	F240, D737, S744, E738, S242, Y735, A747, H750, T753, K721, H757, H754, A732, M733, F713, W734
αRBD+DPP4	−17.3	2.0E-13	H519, T385, L517, D428, P412, D427, P463, K378, C379, G381, S383, R357	D737, S242, D729, T736, Y241, S239, Q714, E237, T251, D725, S720, F730, Q247	A520, P521, T393, L518, F392, L390, E516, Y396, T430, P426, F464, G413, K462, Y380, P384, Y369	E244, W734, P249, T706, Y238, F713, I236, R253, A717, K721, A732, V724
βRBD+DPP4	−20.0	2.2E-15	S477, K462, K484, L452, S349, G446, Q498, S469, T470, D467, Y489, R346, R355, N487, R466, Y421, N460, Y473, K356	F559, R560, E73, Y120, S101, D243, D104, Y105, N103, K71, H748, H100, G99, D96, Y48, N92, R54, N51, E97	G482, V483, G476, F486, F490, A352, Y351, I468, L492, V445, G485, N354, W353, A475, L455, F456, K458, R457	L55, L561, Y752, G741, W629, I102, S245, A743, N74, S93, S745, L49
δRBD+DPP4	−15.9	2.2E-12	Y453, A475, R403, Y505, N487, Y489, R408, D405, R452, T415, K417, Q498	T736, K50, M733, L702, S745, Q731, A732, E244, H757, H750, H754, S239	N501, F497, Y495, G496, Q409, Y473, F456, F490, L492, Y449, G446, G502, T500, L455, G416, G504, V503, Y421	F713, W734, S744, T746, Q749, S720, Y241, P249, K721, A717, F730, V724, T753
κRBD+DPP4	−16.3	1.1E-12	T500, Q498, G446, N501, G496, N450, Y449, S494, K444, F486, T478, K417, Q493, Y505, D405, R403, Y453, Q484	S690, R691, N685, R597, H682, E604, R317, P676, E677, R596, R684, D681, T350	Y489, L455, F456, V445, G485, G482, V483, S477	N694, S686, T600, I319, D678, N679, S642, N321, M348, S349, I295

In the present study, the PDBs used for RBD variants of SARS-CoV-2: wild-type (Wt) = 6LZG (chain B), alpha (α) = 7EKF(chain B), beta (β) = 7WCR(chain A), delta (δ) = 7W9F(chain E) and kappa (κ) = 7SOC(chain B). The PDB used for DPP4 is 4 L72 (chain A).

were located mainly at the surface of the cell membrane (Fig. 1d). The overlay images showed the co-localization of RBD and DPP4 on the cell surface, validating their interaction, which is independent of ACE2 receptor (Fig. 1d).

We overexpressed DPP4 with and without a RBD expressing plasmid by transfection and immunoprecipitated it using DPP4 antibody to support the idea that RBD-DPP4 binding exists. The immunoprecipitated samples were subjected to individual immunoblotting using RBD antibody. Immunoprecipitated sample co-transfected with DPP4 and RBD showed the RBD band following immunoblotting, but the sample expressing only DPP4 without RBD did not display any RBD band (Fig. 1e). Together, our findings showed that DPP4 and RBD created a heterodimer for their stable interaction.

3.4. Binding prediction of WtRBD-DPP4 complex with gliptins

Using molecular docking approach, we have examined some DPP4 inhibitors including sitagliptin, linagliptin, saxagliptin, vildagliptin, and metformin as prospective therapies for SARS-CoV-2 infection in an attempt to prevent viral entry through the DPP4-RBD interaction (Fig. 2a–e; Table 2). Among the tested gliptins, sitagliptin had the lowest dissociation constant (Kd = 1.07E-7 M) and the most favourable B.E. (ΔG = −9.5 kcal/mol) with the WtRBD-DPP4 complex. Linagliptin (ΔG = −8.1 kcal/mol, Kd = 1.1E-6 M) had the second highest binding energy, followed by saxagliptin (ΔG = −7.7 kcal/mol, Kd = 2.24E-6 M), vildagliptin (ΔG = −7.3 kcal/mol, Kd = 4.40E-6 M) and metformin (ΔG = −5.3 kcal/mol, Kd = 1.29E-4 M). In the best-docked pose of sitagliptin with WtRBD-DPP4 complex, sitagliptin bound in between the DPP4 and Wt-RBD complex, in which Y241(A), E244(A), P249(A) residues of DPP4; P463(B) and E516(B) residues of RBD showed hydrophobic interaction with sitagliptin. The R355(B) of RBD formed a hydrogen bond with the fluorine atom of sitagliptin. The favourable binding of WtRBD-DPP4 and sitagliptin (G = −9.5 kcal/mol) was facilitated by their hydrophobic interactions and hydrogen bonding (Fig. 2a). However, in the second most docked pose, sitagliptin interacted with D709 (A), H740(A), N710(A), Y666(A), S630(A), W629(A), S552(A), L554(A) and Y547(A) residues of the catalytic site of DPP4 in WtRBD-DPP4 complex with ΔG = −8.6 kcal/mol (Fig. S3) which is consistent with earlier reports [59]. Other gliptins like linagliptin, saxagliptin, vildagliptin and metformin showed binding interaction with only DPP4 protein in the best-docked pose. Linagliptin formed hydrophobic contacts with G741(A), Y752(A), Y547(A), W629(A), W662(A), W666(A), N710(A), G741(A) residues and hydrogen bonding with S630(A) residue of DPP4, which belongs to the active site of DPP4 (Fig. 2b). Similarly, saxagliptin also showed hydrophobic interaction in the active site with E205(A), E206(A), S209(A), F357(A), Y631(A), Y666(A), Y662(A), N710(A) residues and hydrogen bonding with Y547(A) and S630(A) of DPP4, but with lower B.E. than sitagliptin and linagliptin (Fig. 2c). The vildagliptin showed binding at the middle of α/β-hydrolase domain and β-propeller of DPP4, exhibiting hydrophobic interaction with Y381(A), T401(A), G424(A), P426(A), F516(A), W525(A) and Q586(A) residues and hydrogen bonding with K523(A) residue of DPP4 (Fig. 2d). Among tested gliptins, metformin had the lowest B.E. (−5.3 kcal/mol) with WtRBD-DPP4 due to its smaller size and no aromatic/cyclic groups were present. It binds near to the entrance of DPP4 cavity, at β-propeller site of DPP4 protein, displayed hydrophobic contacts with W124(A), S127 (A), Y128(A), T129(A), Y211(A), Y195(A), I198(A) residues and three hydrogen bonds with Q153(A), N170(A) and D192(A) residues of DPP4 (Fig. 2e). According to the docking analysis, sitagliptin and linagliptin, two of the five gliptins, may be effective in reducing SARS-CoV-2 infection.

3.5. Gliptins maintain the viability of cells

We assessed the cytotoxicity of cultured cells incubated for 48 h in the presence or absence of each ligand in order to examine the impact of the gliptins on the viability of the Vero E6 cell lines. The results demonstrated that, at various doses, none of the inhibitors caused any considerable cell cytotoxicity. We have chosen a range of drug concentrations to investigate the effect of inhibitors on viral multiplication, based on a cell viability of 90 % or more in each well (Fig. 2f–j). The CC_{50} values of sitagliptin, linagliptin, vildagliptin, saxagliptin, and

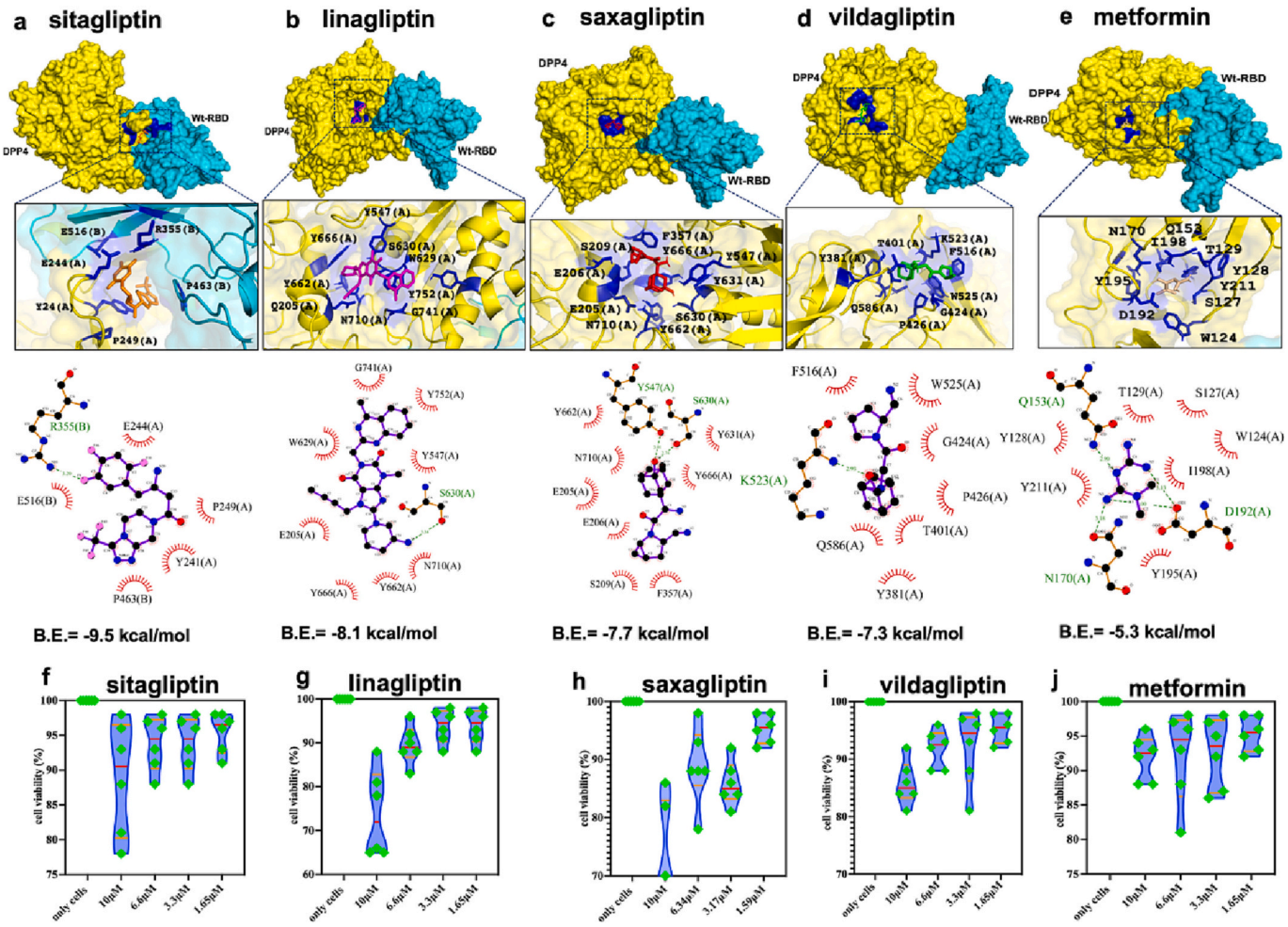

Fig. 2. Wt-RBD-DPP4 complex binding prediction with gliptins. The predicted binding mode of WtRBD-DPP4 complex with a, sitagliptin (orange), b, linagliptin (magenta), c, saxagliptin (red), d, vildagliptin (green), e, metformin (wheat) in best docked pose. The residues were forming the binding pocket shown in dark blue stick representation. The intermolecular hydrophobic contacts were shown in semi-circles, and hydrogen bonds were shown in green dashed lines. f-j, The effect of gliptins on cellular cytotoxicity was measured at different concentration. Data showed average values ± S.D. of three repeated experiments and six biological replicates ± S.D. were displayed here. (For interpretation of the references to colour in this figure legend, the reader is referred to the web version of this article.)

metformin were 67.36 μM, 21.28 μM, 130.81 μM, 21.06 μM, and 46.29 μM, respectively (Table 4).

3.6. Selected gliptins can encumber the Wt-SARS-CoV-2 infection

The preceding sections predicted that impeding DPP4 may be therapeutically advantageous for the treatment of SARS-CoV2 infection. Therefore, we tested DPP4 inhibitors to determine whether they could encumber the SARS-CoV-2 infection in vitro. We infected Vero E6 cells with Wt-SARS-CoV-2 and treated them with sitagliptin, linagliptin, vildagliptin, saxagliptin, and metformin alone. We have found that sitagliptin and linagliptin, two of the DPP4 inhibitors, have demonstrated the greatest potential in terms of lowering viral replication with IC_{50} value of 1.46 μM and 2.21 μM, respectively (Fig. 3a and Table 4). Sitagliptin at the concentration of 1.98 μM can significantly abrogated the virus growth, whereas linagliptin had a similar inhibitory efficacy at a concentration of 1.06 μM. We were unable to identify any inhibitory efficacy of metformin, vildagliptin, or saxagliptin, even at higher concentrations (Fig. 3a). We also demonstrated that sitagliptin, at a concentration of 0.99 μM, partially encumbered the viral growth; however, at a concentration of 1.98 μM, it can significantly inhibited viral multiplication by almost six folds compared to cells with virus alone. This is very similar to the inhibitory efficacy of remdesivir (Fig. 3a,b). Linagliptin, likewise remdesivir, halted the multiplication of viruses at a minimum concentration of 1.06 μM (Fig. 3a,b). However, we have found that sitagliptin and linagliptin in combination had an inhibitory efficacy better than the remdesivir; even at lower concentration levels of 0.99 μM and 1.06 μM, respectively, sitagliptin and linagliptin suppressed viral proliferation significantly by 10 folds (Fig. 3b).

3.7. Selected gliptins refuted the cell surface interaction of DPP4-RBD

We used confocal microscopy to carry out a cell-surface binding assay to clarify the impact of gliptins on the interaction between the Wt-RBD-Fc and DPP4 in ACE2 knockout cells. We have already shown the ACE2 independent DPP4 interaction with RBD-Fc (Fig. 1d, 3c). However, sitagliptin treatment prevented the co-localization of RBD-Fc with DPP4 (Fig. 3c). Similarly, linagliptin treatment hampered the formation of a DPP4-RBD heterodimer complex. The interaction between RBD and DPP4 at the cell membrane, which is necessary for viral entry into cells, was prevented when both the gliptins were provided together in ACE2 knockout cells (Fig. 3c).

We overexpressed DPP4 except panel 6 with RBD expressing plasmid by transfection and immunoprecipitated it using DPP4 antibody to support the idea that RBD-DPP4 binding exists (Fig. 3d). In panel 6, we expressed only RBD expressing plasmid in DPP4 knockout cells. The immunoprecipitated samples using DPP4 antibody were subjected to individual immunoblotting using RBD antibody. Immunoprecipitated

Table 2
Molecular docking analysis of gliptins with RBD(variants)-DPP4 complex, WtRBD-ACE2 complex and PLpro using AutoDock Vina.

Compound	Protein	Binding affinity ΔG (kcal/mol)	Dissociation constant Kd (M) at 25.0 °C	Residues involved in the intermolecular H–bonding interactions			Residues involved in intermolecular hydrophobic contacts
				Residue	Atom*	Distance (Å)	
Linagliptin	WtRBD-DPP4	−8.1	1.14E-6	S630(A)	NH: O	3.3	G741(A), Y752(A), Y547(A), W629(A), Y662(A), Y666(A), N710(A), G741(A)
Sitagliptin	WtRBD-DPP4	−9.5	1.07E-7	R355(B)	NH:F	3.2	Y241(A), E244(A), P249(A), P463(B), E516(B)
Vildagliptin	WtRBD-DPP4	−7.3	4.40E-6	K523 (A)	NH:O	2.9	Y381(A), T401(A), G424(A), P426(A), F516(A), W525(A), Q586(A)
Saxagliptin	WtRBD-DPP4	−7.7	2.24E-6	Y547 (A) S630(A)	OH:O OH:O	3.0 2.7	E205(A), E206(A), S209(A), F357(A), Y631(A), Y666(A), Y662(A), N710(A)
Metformin	WtRBD-DPP4	−5.3	1.29E-4	Q153 (A) N170 (A) D192 (A)	NH:N CO:HN CO:HN CO:HN	2.9 3.2 3.1 3.0	W124(A), S127(A), Y128(A), T129(A), Y211(A), Y195(A), I198(A)
Linagliptin	αRBD-DPP4	−8.2	9.61E-7	T251 (A) R253 (A)	NH:N NH: OH NH:N	3.0 2.9 3.2	Y248(A), P249(A), K250(A), W353(B), P463(B), F464(B), E465(B), R466(B)
Sitagliptin	αRBD-DPP4	−8.2	9.61E-7	E205(A) E206(A) Y547 (A) S630(A) H740 (A)	CO:HN CO:HN OH:F OH:N NH:N	3.3 3.3 3.1 2.7 3.2	S209(A), F357(A), Y662(A)
Linagliptin	βRBD-DPP4	−8.7	4.13E-7	E205(A)	CO:HN	3.0	E206(A), F357(A), Y547(A), K554(A), W629(A), S630(A), Y662(A), Y666(A), T478(B), P479(B), F486(B)
Sitagliptin	βRBD-DPP4	−9.4	1.27E-7	T478(B)	OH:N	3.0	Y547(A), K554(A), N562(A), W563(A), W629(A), Y752(A), P479(B) N487(B)
Linagliptin	δRBD-DPP4	−7.8	1.89E-6	–	–	–	Y48, R560(A), L561(A), N562(A), W627(A), W629(A), V653(A), G741 (A), I742(A), I751(A), Y752(A)
Sitagliptin	δRBD-DPP4	−9.2	1.77E-7	Q527 (A)	NH:N	3.1	D545(A), K554(A), R560(A), N562(A), W627(A), W629(A), G741(A), Y752(A)
Linagliptin	κRBD-DPP4	−8.7	4.13E-7	Q553 (A)	CO: HN	2.9	Y547(A), W627(A), W629(A), V653(A), G741(A), I751(A), Y752(A)
Sitagliptin	κRBD-DPP4	−8.8	3.49E-7	G355 (A) S376(A)	NH:N NH:F	2.9 3.3	E347(A), M348(A), S349(A), T351(A), V354(A), E378(A), G380(A), D588(A)
Linagliptin	WtRBD-ACE2	−6.0	3.95E-5	–	–	–	P321(A), N322(A), T324(A), G354(A), M383(A), A386(A), A387(A), R403(B), D405(B), Y505(B)
Sitagliptin	WtRBD-ACE2	−7.2	5.21E-6	N103 (A)	NH:F	3.1	Q98(A), Q101(A), Q102(A), N194(A), Y196(A), E208(A)

Here, the PDB used for variants of RBD: wild-type = 6LZG (chain B), alpha = 7EKF(chain B), beta = 7WCR(chain A), delta = 7W9F(chain E) and kappa = 7SOC(chain B). The PDB used for DPP4 and WtRBD-ACE2 are 4 L72 (chain A) and 6LZG, respectively.
* The atoms on right represent ligand atoms and on the left represent protein residue atoms.

sample co-transfected with DPP4 and RBD showed the RBD band following immunoblotting, but the sample expressing only DPP4 without RBD did not display any RBD band. Together, our findings showed that DPP4 and RBD created a heterodimer for their stable interaction (Fig. 3d). In presence of gliptins, we didn't observe any RBD band, which clearly indicated that gliptins inhibited DPP4 activity and disrupts DPP4-RBD interaction.

3.8. Effect of gliptins on cells viability and DPP4 enzymatic activity

The cells infected with Wt-SARS-CoV-2 caused >40 % cell cytotoxicity, however, the effect of gliptins on cytotoxicity of infected cells reduced to 10 % was measured at different concentration. Around 90 % virus infected cells were remained viable after sitagliptin or linagliptin or its combinatorial treatment. The viability of infected cells after gliptins treatment even better than infected cells treated with remdesivir (Fig. 3e). We further observed that virus infection augmented cellular DPP4 enzymatic activity which was significantly reduced in treatment with sitagliptin and linagliptin or their combination (Fig. 3f). The abrogation of DPP4 enzymatic in infected cells by gliptins were dose dependent as higher concentration of any of gliptins inhibited more DPP4 activity than their respective lower concentration. Remdesivir treatment in infected cells did not affect the DPP4 activity. DPP4 knockout cells (KO) cells also did not show any DPP4 activity due to absence DPP4 gene (Fig. 3f).

3.9. MD simulation of WtRBD-DPP4 in presence of linagliptin or sitagliptin

Using the live Wt-SARS-CoV-2 virus in our experiments and microscopy study, we established that sitagliptin and linagliptin were able to diminish SARS-CoV-2 infection. Additionally, we were interested in learning how specific gliptins prevented SARS-CoV-2 infection. In this context, we have performed the MD simulation of sitagliptin and linagliptin with the WtRBD-DPP4 complex. To study the impact of inhibitors on the DPP4 structure without Wt-RBD, we performed MD simulations of DPP4 alone in the absence and presence of linagliptin and sitagliptin (Fig. 3d–g). Initially, the RMSD, SASA, R_g, and RMSF in DPP4 were

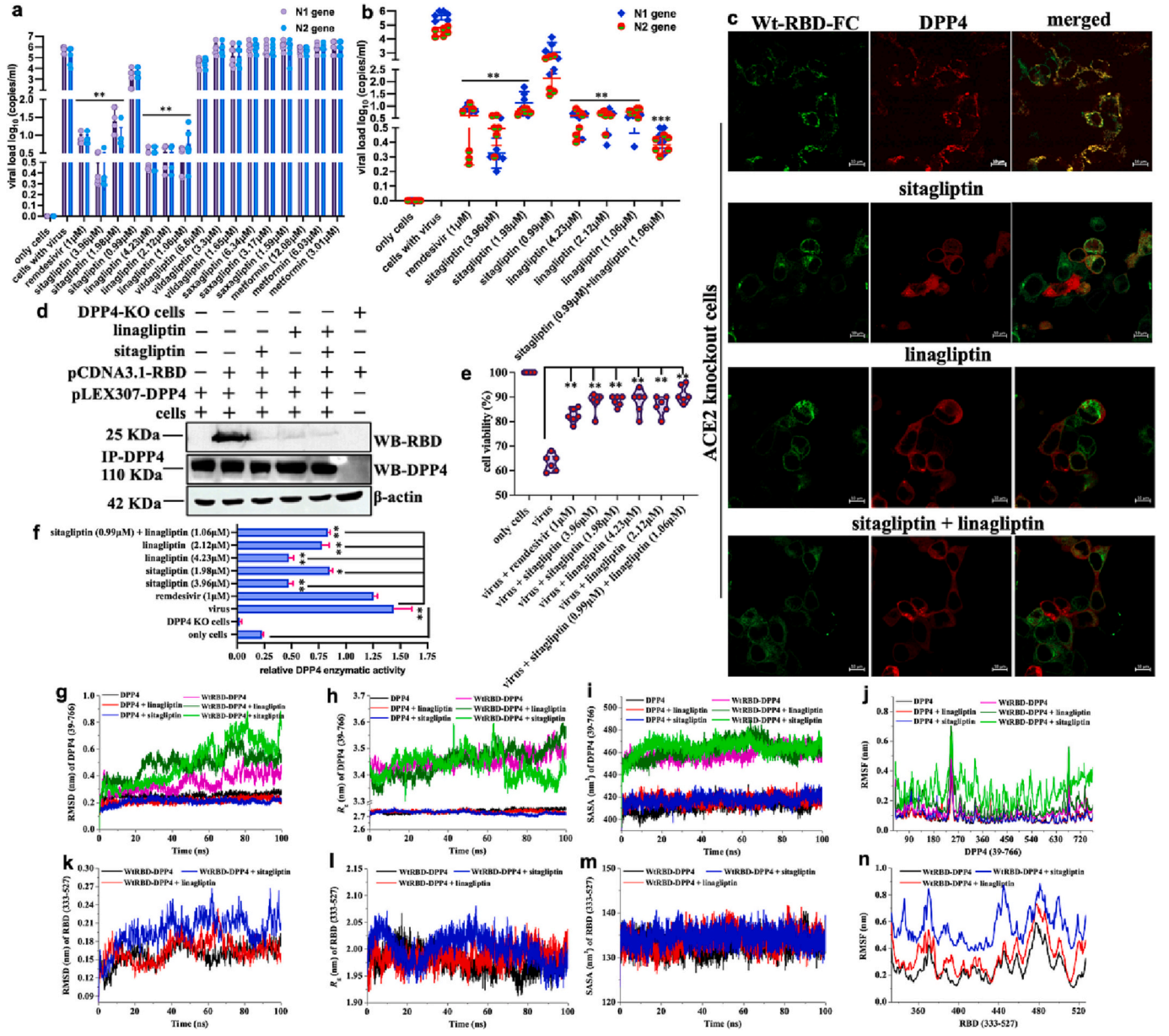

Fig. 3. Efficacy of gliptins against SARS-CoV-2 infection. a, Effect of selected gliptins at different concentrations on Wt-SARS-CoV-2 infection was studied. b, Effect of sitagliptin and linagliptin alone or in their combination was checked to impede the SARS-CoV-2 infection in vitro. In both figure a and b, remdesivir was used as a reference anti-viral compound. The viral load was represented as an average of triplicate data, and six biological replicates ± S.D. were displayed here. The significance of viral load reduction was measured, *p*-values ** < 0.01; and *** < 0.001 were considered statistically significant. c, Confocal imaging was performed to evaluate the co-localization of Wt-RBD-Fc with DPP4 in the absence and presence of sitagliptin, linagliptin, or their combination in ACE2 knockout cells. d, Calu-3 cells were transfected with DPP4 expressing pLEX307-DPP4 except lane 6 where DPP4-KO cells were used. Similarly, pCDNA3.1-RBD was co-transfected in all lanes except lane 1 in the presence or absence of sitagliptin or linagliptin. All samples were immunoprecipitated with DPP4 antibody, and immunoblotted with RBD antibody. β-actin was used as an internal control. e, The effect of gliptins on viability of infected cells was measured at different concentration. Data showed average values ± S.D. of three repeated experiments and six biological replicates ± S.D. were displayed here. f, Only cells, DPP4 knockout cells (KO), virus infected cells, infected cells treated with remdesivir or gliptins were tested for DPP4 enzymatic activity. Throughout the simulation, the stability of the DPP4 (39–766) structure was evaluated by calculating its g, Root-mean-square deviation (RMSD), h, Radius of gyration (R_g), i, Solvent-accessible surface area (SASA), and j, Root-mean-square fluctuation (RMSF) for the following systems: DPP4, DPP4 + linagliptin, DPP4 + sitagliptin, WtRBD-DPP4, WtRBD-DPP4 + linagliptin and WtRBD-DPP4 + sitagliptin. k, RMSD, l, R_g, m, SASA and n, RMSF of Wt-RBD (333–527) structure were calculated for the following systems: WtRBD-DPP4, WtRBD-DPP4 + linagliptin, and WtRBD-DPP4 + sitagliptin.

analysed for three systems: DPP4, DPP4 + linagliptin and DPP4 + sitagliptin, which depicted that linagliptin and sitagliptin didn't induce any conformational instability to DPP4 in the absence of WtRBD, as there were no significant changes in the positions of atoms (RMSD and RMSF), the R_g as well as SASA of DPP4 in presence of linagliptin and sitagliptin during the simulation (Fig. 3d–g, Fig. S4a–c). Whereas, with the addition of Wt-RBD to the DPP4 system, the RMSD of DPP4 significantly elevated from 0.25 ± 0.02 nm to 0.35 ± 0.07 nm (Fig. 3d). When Wt-RBD was present, DPP4's RMSD was increase to alter the interactions between the two large proteins and established a stable Wt-RBD-DPP4 complex. After 70 ns, the RMSD was stabilised, indicating that Wt-RBD and DPP4 have formed a stable complex (Fig. 3d). The RMSD of DPP4 complexed with Wt-RBD was considerably increased to 0.49 ± 0.16 nm in the presence of sitagliptin, although the RMSD of

DPP4 alone with sitagliptin was only 0.12 ± 0.02 nm (Fig. 3d, Fig. S4a). Furthermore, sitagliptin impaired the structure of Wt-RBD in the WtRBD-DPP4 complex by increasing its RMSD to 1.33-fold, which was considerably higher (Fig. 3h, Fig. S4d). The RMSD results thus indicated that sitagliptin substantially destabilized the WtRBD-DPP4 complex. The RMSD of DPP4 attached with Wt-RBD increased to 2.17 folds in the presence of linagliptin, which was considerably greater than DPP4 alone with linagliptin (Fig. 3d, Fig. S4a). The fact that the RMSD of the Wt-RBD of the heterodimer complex increased by nearly two folds when linagliptin was present, suggested that the RBD became unstable (Fig. 3h). In Movie S2, simulation of WtRBD-DPP4 in the presence of sitagliptin illustrated how the drug interfered with the binding of DPP4 and WtRBD. The two residues of DPP4 (Q731 and E244) were involved in hydrogen bonding with two residues of WtRBD (G381, R355) having bond distance 1.9 and 1.7 Å, respectively, at the initial time of the simulation. These hydrogen bonds were also observed in the molecular docking study of DPP4 with WtRBD. In the simulation, sitagliptin pushed the Wt-RBD away from DPP4 by interacting with the Wt-RBD, which broke the hydrogen bonds between them. At the end of the simulation, the distance of hydrogen bonds between two residues had increased to > > 3.5 Å. Likewise, in the simulation of WtRBD-DPP4 with linagliptin, the hydrogen bond between DPP4 residues (E244 and T736) and Wt-RBD residues (R355 and L517) was disrupted by linagliptin (Movie S3). Throughout the simulation, linagliptin interacted strongly with DPP4, which enabled the separation of DPP4 from Wt-RBD. Further, we have studied the compactness of WtRBD-DPP4 in the presence and absence of gliptins by calculating the radius of the gyration (R_g) parameter. In the absence of Wt-RBD, the average R_g value of DPP4 alone is 2.74 ± 0.01 nm, whereas the average R_g value of DPP4 in presence of Wt-RBD was increased to 3.45 ± 0.03 nm (Fig. 3e, Fig. S4b) indicated the instability of DPP4 in presence of Wt-RBD. In the presence of sitagliptin and linagliptin, the average R_g value of DPP4 in WtRBD-DPP4 complex is 3.44 ± 0.04 nm and 3.45 ± 0.05 nm, respectively, which implies that neither sitagliptin nor linagliptin altered the radius of gyration of DPP4 in the presence of Wt-RBD (Fig. 3e, Fig. S4b). We assessed the SASA of WtRBD-DPP4 to advance our understanding of the compactness of the complex after gliptin treatment. The average SASA value of only DPP4 was 412.31 ± 4.99 nm^2 which was significantly increased to 458.15 ± 5.44 nm^2 in presence of Wt-RBD (Fig. 3f, Fig. S4c). The significantly higher SASA value of DPP4 in the presence of Wt-RBD demonstrated that the structure of DPP4 lost its compactness and stability in the presence of Wt-RBD, enhancing the structure's accessibility to solvents. Intriguingly, sitagliptin and linagliptin caused the average SASA value of DPP4 in WtRBD-DPP4 to increase to 464 ± 6.02 nm^2 and 461.88 ± 7.75 nm^2, respectively. Additionally, we noticed a little rise in the SASA of Wt-RBD when sitagliptin and linagliptin were present. The aforementioned finding indicates that gliptins weakened the structural stability the WtRBD-DPP4 complex (Fig. 3f). To examine the conformational fluctuations that occurred in DPP4 during simulation, the RMSF of each residue of DPP4 in the presence of Wt-RBD was evaluated. In the WtRBD-DPP4 complex, the average RMSF value of DPP4 fluctuated by ~0.13 ± 0.05 nm, while the DPP4 alone system was found to fluctuate at an average of ~0.09 ± 0.06 nm (Fig. 3g). Higher fluctuations were observed in DPP4 in the presence of Wt-RBD specifically at the N-terminus (87–235 aa) and C-terminus region (564–766 aa) of DPP4 which is the binding domain of Wt-RBD. In presence of sitagliptin and linagliptin, the RMSF value had increased to 0.27 ± 0.09 nm and 0.16 ± 0.08 nm, respectively (Fig. 3g). Likewise, the average RMSF of Wt-RBD increased significantly from 0.26 ± 0.10 to 0.55 ± 0.12 nm when sitagliptin was present. Sitagliptin significantly affected the destabilization of DPP4 and WtRBD, as evidenced by the 2.5-fold rise in RMSF that was seen in each of the residues of DPP4 and Wt-RBD (Fig. 3k). In addition, linagliptin enhanced the average RMSF value of Wt-RBD from 0.26 ± 0.10 nm to 0.35 ± 0.13 nm (Fig. 3k). According to the RMSF results, both sitagliptin and linagliptin caused more conformational instability to both DPP4 and Wt-RBD. Moreover, we have calculated the binding free energy (ΔGbinding) of sitagliptin and linagliptin with WtRBD-DPP4 complex by using MM–PBSA analysis (Table 3). The $\Delta G_{binding}$ for WtRBD-DPP4 with sitagliptin and linagliptin was calculated to be −65.16 ± 0.86 kcal/mol and − 60.76 ± 0.73 kcal/mol, respectively. The MM-PBSA data highlighted that van der Waal energy and non-polar solvation energy contributes maximum to the favourable $\Delta G_{binding}$ of sitagliptin and linagliptin with WtRBD-DPP4 complex. It can be speculated that the strong binding affinity of sitagliptin and linagliptin with WtRBD-DPP4 complex results into the escalation of RMSD, RMSF and SASA value of DPP4 and Wt-RBD proteins, leading to the destabilization of WtRBD-DPP4 complex.

3.10. Binding prediction of DPP4 with the RBD of VOCs

Since pandemic started, different variants of SARS-CoV-2 have been rapidly evolving throughout the world. Since DPP4 has emerged as a promising therapeutic target to prevent SARS-CoV-2 infection, we have also examined DPP4's ability to bind to other SARS-CoV-2 variants, including VOCs: α-RBD (N501Y), β-RBD (K417N, E484K and N501Y), δ-RBD (T478K and L452R) and κ-RBD (E484Q and L452R) (Fig. S5). The B.E. of DPP4 with alpha, beta, delta and kappa RBD was −17.3, −20.0, −15.9 and −16.3 kcal/mol, respectively, in the best docked pose. The major residues VOCs involved in binding with DPP4 are summarised in Table 1. Among VOCs, specifically α-RBD, δ-RBD and κ-RBD preferentially bound to the external side of the α/β-hydrolase domain (506–766) of DPP4 (Fig. S5). The binding site of α-RBD with DPP4 was almost similar to Wt-RBD i.e. α/β-hydrolase domain of DPP4. However, the B.E. of αRBD-DPP4 complex (−17.3 kcal/mol) was higher than WtRBD-DPP4 complex (−14.9 kcal/mol) due to increased dipole–dipole interaction between α-RBD (28 residues) and DPP4 (25 residues). Interestingly, only β-RBD entered inside the cavity of DPP4, in which 37 residues spanning 357–521 domain of β-RBD interacted with 32 residues majorly from the β-propeller domain of DPP4, through hydrophobic interaction and hydrogen bonding, that leads to highest binding affinity (−20 kcal/mol) and lowest Kd value of 2.0E-13 M among VOCs. Notably, the mutated residue K484 of β-RBD also participated in hydrogen bonding with Y120 residue of DPP4 (Fig. S5b).

The δ-RBD is double mutated derivative of Wt-RBD comprising T478K and L452R mutations. Interestingly, R452 residue of δ-RBD interacted with E244 residue of DPP4. Along with that, total 30 residues spanning 403–505 domain of δ-RBD showed dipole-dipole and hydrophobic interactions with 25 residues spanning 50, 702–757 and 241–244 domain of DPP4 (Fig. S5c). Similarly, 26 residues spanning 403–505 of κ-RBD interacted with 24 residues spanning 295–350, a 597 residue and 600–694 domain of DPP4. The mutated residue, Q484 in κ-RBD formed a hydrogen bond with T350 of DPP4 (Fig. S5d). The findings indicated that DPP4 has a remarkable ability to attach to each VOCs of the SARS-CoV-2 spike protein.

3.11. Binding prediction of sitagliptin/linagliptin with the RBD(VOCs)-DPP4 complex

We next studied the binding potential of sitagliptin and linagliptin with VOCs of SARS-CoV-2 spike protein by molecular docking method (Fig. 4a–h; Table 2). Surprisingly, sitagliptin and linagliptin's binding sites with αRBD-DPP4 differed from those we found with WtRBD-DPP4, but both gliptins exhibited similar binding energies (−8.2 kcal/mol) and Kd value (9.61E-7 M) with αRBD-DPP4. Sitagliptin displayed hydrophobic interaction with S209(A), F357(A), and Y662(A) residues as well as hydrogen bonds with E205(A), E206(A), Y547(A), S630(A) and H740 (A) residues situated at the centre of β-propeller and α/β-hydrolase domain of DPP4 (Fig. 4a). Linagliptin, in fact, had hydrophobic interaction with Y248(A), P249(A), Lys250(A), W353(B), P463(B), F464(B), E465(B), R466(B) residues and hydrogen bonding with T251(A), R253 (A) residues near to the binding site αRBD and DPP4 (Fig. 4e). The main intermolecular forces between sitagliptin/linagliptin and the RBD-DPP4

Table 3
The calculated binding free energy ($\Delta G_{binding}$) for sitagliptin and linagliptin with WtRBD-DPP4, WtRBD-ACE2 and PLpro using the molecular mechanics Poisson Boltzmann surface area (MM–PBSA).

Energy components (kcal/mol)	WtRBD-DPP4 + sitagliptin	WtRBD-DPP4 + linagliptin	WtRBD-ACE2 + sitagliptin	WtRBD-ACE2 + linagliptin
ΔE_{vdw}	−42.02 ± 1.27	−43.26 ± 1.34	−33.85 ± 3.14	−53.96 ± 0.32
ΔE_{elec}	−14.91 ± 1.06	−2.66 ± 0.82	−6.37 ± 3.33	−3.05 ± 0.15
ΔE_{MM} [a]	−56.93 ± 1.16	−45.92 ± 1.08	−40.22 ± 6.47	−57.01 ± 0.47
ΔG_{ps}	26.25 ± 1.18	17.87 ± 1.41	18.24 ± 2.70	23.34 ± 0.19
ΔG_{nps}	−34.48 ± 3.45	−32.71 ± 1.66	−28.45 ± 3.65	−44.31 ± 0.72
ΔG_{solv} [b]	−8.23 ± 2.27	−14.84 ± 0.33	−10.21 ± 0.95	−33.67 ± 0.53
$\Delta G_{binding}$ [c]	**−65.16 ± 0.86**	**−60.76 ± 0.73**	**−50.43 ± 4.88**	**−77.97 ± 0.84**

[a] $\Delta EMM = \Delta Evdw + \Delta Eelec$.
[b] $\Delta G_{solv} = \Delta G_{ps} + \Delta G_{nps}$.
[c] $\Delta G_{binding} = \Delta E_{MM} + \Delta G_{solv}$.

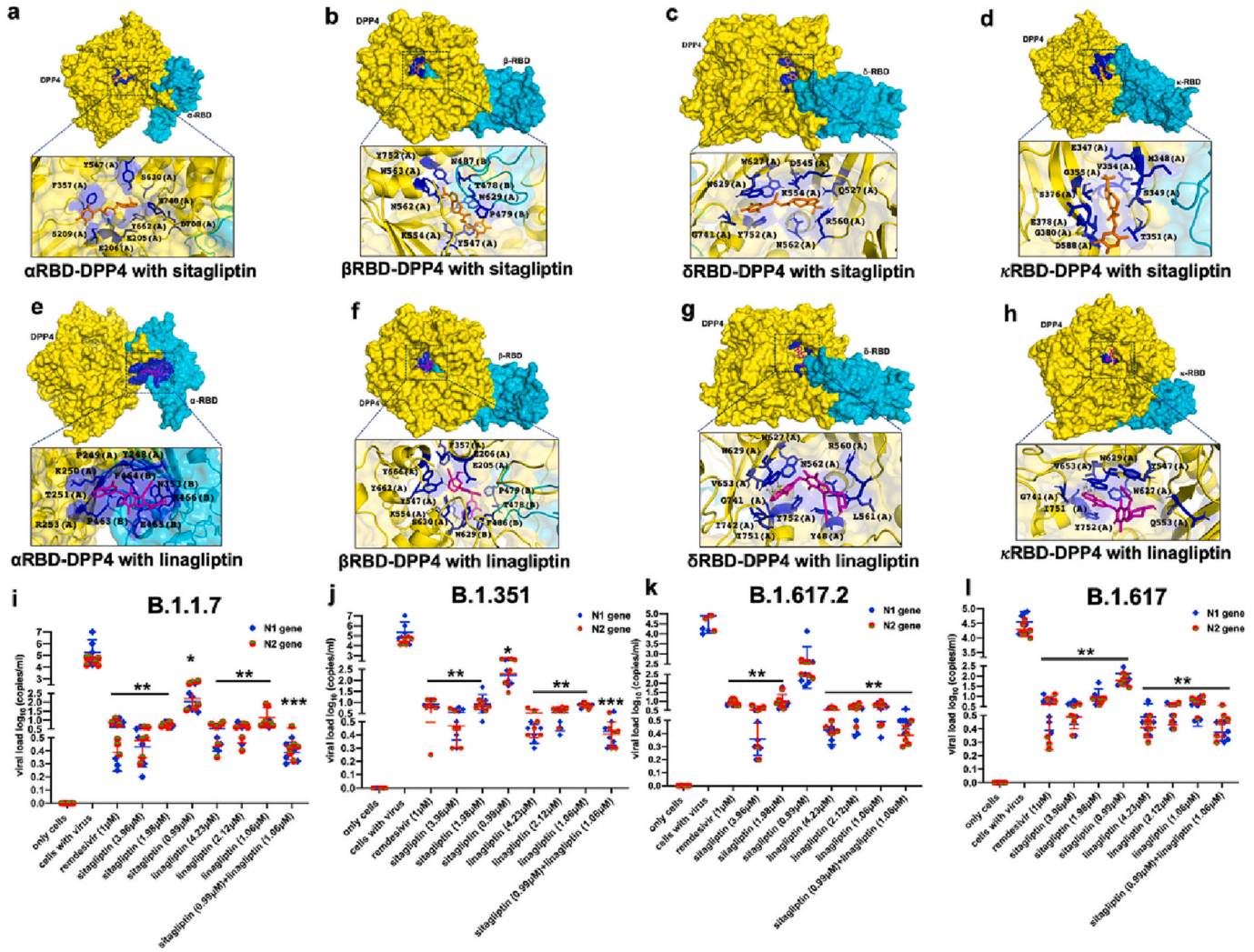

Fig. 4. The binding and molecular interactions of the gliptins with RBD-DPP4 complex of VOCs. a–h, The best-docked poses of sitagliptin and linagliptin with αRBD-DPP4, βRBD-DPP4, δRBD-DPP4 and κRBD-DPP4 complexes illustrated here. The sitagliptin and linagliptin were represented by orange and magenta stick respectively. The residues forming the binding pocket were shown in dark blue stick. i–l, The effect of sitagliptin and linagliptin alone or in combination on numerous VOCs was investigated here. Remdesivir was used as a reference anti-viral compound. The viral load was represented as an average of triplicate data, and six biological replicates ± S.D. were displayed here. The significance of viral load reduction was measured, *p*-values ** < 0.01; and *** < 0.001. Two different set of primers (N1, and N2) of nucleocapsid gene of SARS-CoV-2 were used for RT-qPCR. (For interpretation of the references to colour in this figure legend, the reader is referred to the web version of this article.)

complex were the hydrophobic interaction and hydrogen bonding.

In the case of the βRBD-DPP4 complex (Fig. 4b, f), sitagliptin and linagliptin bound at the 487–752 domain and 205–666 domain of DPP4 with the B.E. of −9.4 kcal/mol; −8.7 kcal/mol and Kd value of 1.27E-7 M; 4.13E-7 M, respectively (Table 2). With δRBD-DPP4 complex, sitagliptin (B.E. = −9.2 kcal/mol, Kd = 1.77E-7 M) and linagliptin (B.E. = −7.8 kcal/mol, Kd = 1.89E-6 M) showed interaction with 527–752 aa and 48, 560–629 aa of the α/β-hydrolase domain of DPP4, respectively, were mainly driven by van der Waal interactions. Remarkably, sitagliptin showed more binding interaction with δRBD-DPP4 than

linagliptin (Fig. 4c,g, Table 2).

Furthermore, in the case of the κRBD-DPP4 complex, sitagliptin displayed binding in the β-propeller domain spanning residues 347–380 and 588 of α/β-hydrolase domain of DPP4 with B.E. = −8.8 kcal/mol and Kd = 3.49E-7 M (Fig. 4d). Contrarily, linagliptin had shown its binding in the α/β-hydrolase domain of DPP4, spanning residues 547–751, with B.E. = −8.7 kcal/mol and Kd = 4.13E-7 M (Fig. 4h; Table 2). Sitagliptin and linagliptin had significantly strong binding interactions with all RBD (variants)-DPP4 complexes, with B.E. ranging from −7.8 to −9.4 kcal/mol. Based on their RBD-DPP4 complex binding profiles, sitagliptin and linagliptin may be effective therapeutic options for mitigating various SARS-CoV2 variants.

3.12. Gliptins inhibits SARS-CoV-2 VOCs infection

The preceding sections decisively established how inhibiting DPP4 significantly reduce Wt-SARS-CoV-2 infection in an in vitro system (Fig. 3a, b). These findings inspired us to check the therapeutic benefits of gliptins against SARS-CoV-2 VOCs. Therefore, we infected Vero E6 cells with B1.1.7, B.1.351, B.1.617.2, and B.1.617.1 variants separately and treated with sitagliptin, or linagliptin alone or in their combination. Sitagliptin and linagliptin had demonstrated to be extremely promising in preventing the proliferation of the virus among variants we tested. Sitagliptin at the concentration 0.99 μM could partially inhibit α-SARS-CoV-2, β-SARS-CoV-2, κ-SARS-CoV-2 (Fig. 4i,j,l) but was unable to prevent even the partial growth of δ-SARS-CoV-2 variant (Fig. 4k). Linagliptin showed a dose-dependent inhibitory effectiveness against all VOCs (Fig. 4i–l). At a concentration of 1.98 μM, sitagliptin could significantly impede viral growth by nearly 6–7 folds among all variants (Fig. 4i–l). The sitagliptin showed IC_{50} value against variants of SARS-CoV-2 (B1.1.7, B.1.351, B.1.617.2, and B.1.617.1) ranges from 1.64 to 1.89 μM. Similarly, linagliptin showed IC_{50} value in range 1.92 to 2.32 μM (Table 4).

We further checked in combination of these two drugs and found that sitagliptin and linagliptin even at lower concertation of 0.99 μM and 1.06 μM respectively abrogated the viral growth (Fig. 4i–l). Nevertheless, at the lowest dose in our study, the combinatorial treatment was able to significantly halt the proliferation of all variants. Combinatorial sitagliptin and linagliptin at the lowest dose or sitagliptin and linagliptin alone at their highest doses were observed to entirely prevent the infection of all clades. This inhibitory efficacy of gliptins was even more effective than that of remdesivir among all VOCs.

3.13. Binding prediction of sitagliptin/linagliptin with ACE2 receptor

Since the N53, N90, N103, N322, N432, N546, and N690 glycosylation of ACE2 is essential for viral entry, we explored the compatibility of sitagliptin and linagliptin for binding with the WtRBD-ACE2 complex [60,61]. In the molecular docking analysis, linagliptin with B.E. = −6.0 kcal/mol and Kd = 3.95E-5 M, displayed hydrophobic contacts with residues spanning 321–505 present at the extracellular domain of ACE2 (Fig. 5a,b; Table 2). The binding location of linagliptin was close to the binding site of Wt-RBD with ACE2. However, the sitagliptin showed interaction in 98–208 domain of ACE2 with B.E. = −7.2 kcal/mol and Kd = 5.21E-6 M (Fig. 5a,b; Table 2). Moreover, sitagliptin and the N103 residue of the ACE2 receptor established a hydrogen bond (3.1 Å), and linagliptin formed hydrophobic contact with N322 of ACE2. It's worth noting that these two drugs, linagliptin and sitagliptin, were coupled to the ACE2 receptor's N322 and N103 glycosylation sites, respectively, might be blocking ACE2-RBD binding and SARS-CoV-2 entry.

3.14. MD simulation of gliptins with ACE2 receptor

Moreover, the detailed binding mechanism of sitagliptin and linagliptin with WtRBD-ACE2 complex was studied by using molecular dynamics simulation. In the WtRBD-ACE2 + sitagliptin system, the bonding between sitagliptin and N103 (glycosylation site of ACE2) remained uninterrupted throughout the simulation, which was driven by weak van der Waal interactions (Fig. 5c). Similarly, linagliptin was seen in contact with a glycosylation site, N322 of ACE2 (Fig. 5c). We have evaluated the $\Delta G_{binding}$ of linagliptin and sitagliptin with WtRBD-ACE2 using the MM-PBSA method, which was found to be −77.97 ± 0.84 kcal/mol and − 50.43 ± 4.88 kcal/mol respectively (Table 3). Both sitagliptin and linagliptin was bound to WtRBD-DPP4 and WtRBD-ACE2 with a significantly higher binding energy. The van der Waal interaction and non-polar solvation energy were the two primary forces that strongly influenced the favourable binding energy. The results demonstrated that both linagliptin and sitagliptin may prevent the ACE2 receptor from getting glycosylated by blocking glycosylation sites, which might be a beneficial strategy to prevent ACE2-spike binding.

3.15. Cell-surface binding of RBD to ACE2

To elucidate the role of gliptins in impeding the interaction between the Wt-RBD and ACE2, we performed RBD-ACE2 binding assay. Transfected GFP-RBD was fused with alexa-fluor 647 labelled-secondary antibody specific to ACE2 in Calu-3 cells. Confocal microscopic images subsequently showed that ACE2 was located mainly at the cell membrane (Fig. 5d). GFP-RBD-positive cells were stained with alexa-fluor 647 labelled-ACE2, and the overlay images showed the co-localization of RBD and ACE2 on the cell surface, validating their interaction (Fig. 5d). However, in the presence of sitagliptin, linagliptin or their combination hampered the interaction of ACE2 with RBD (Fig. 5d).

We overexpressed myc-ACE2 with and without a RBD expressing plasmid by transfection and immunoprecipitated it using myc antibody to support the idea that RBD-ACE2 binding exists. The immunoprecipitated samples were immunoblotted separately using RBD and ACE2 antibodies. Immunoprecipitated samples co-transfected with myc-ACE2 and RBD showed the RBD band following immunoblotting with RBD antibody, but the sample expressing only ACE2 without RBD did not display any RBD band (Fig. 5e). Together, our findings showed that ACE2 and RBD created a heterodimer for their stable interaction. However, in the presence of gliptins individually or in combination, disavowed to form a heterodimer complex of RBD and ACE2 (Fig. 5e).

3.16. PLpro, Ulp1, PLpro gel-based assay substrate expression, and purification

The induced protein expression for His-SUMO-PLpro was checked by running SDS-PAGE gel (12 %) and the expressed protein (mol. wt. ≈

Table 4
The CC_{50} and IC_{50} values of gliptins obtained from cell viability assay and SARS-CoV-2 inhibition assay, respectively.

S·No	Drug	CC_{50} value (μM)	IC_{50} value (μM)				
			Wt-SARS-CoV-2	B.1.1.7	B.1.351	B.1.617.2	B.1.617
1	Sitagliptin	67.36	1.46	1.64	1.65	1.84	1.89
2	Linagliptin	21.28	2.21	1.95	1.92	2.32	2.27
3	Vildagliptin	130.81	3.83	–	–	–	–
4	Saxagliptin	21.06	6.68	–	–	–	–
5	Metformin	46.29	10.49	–	–	–	–

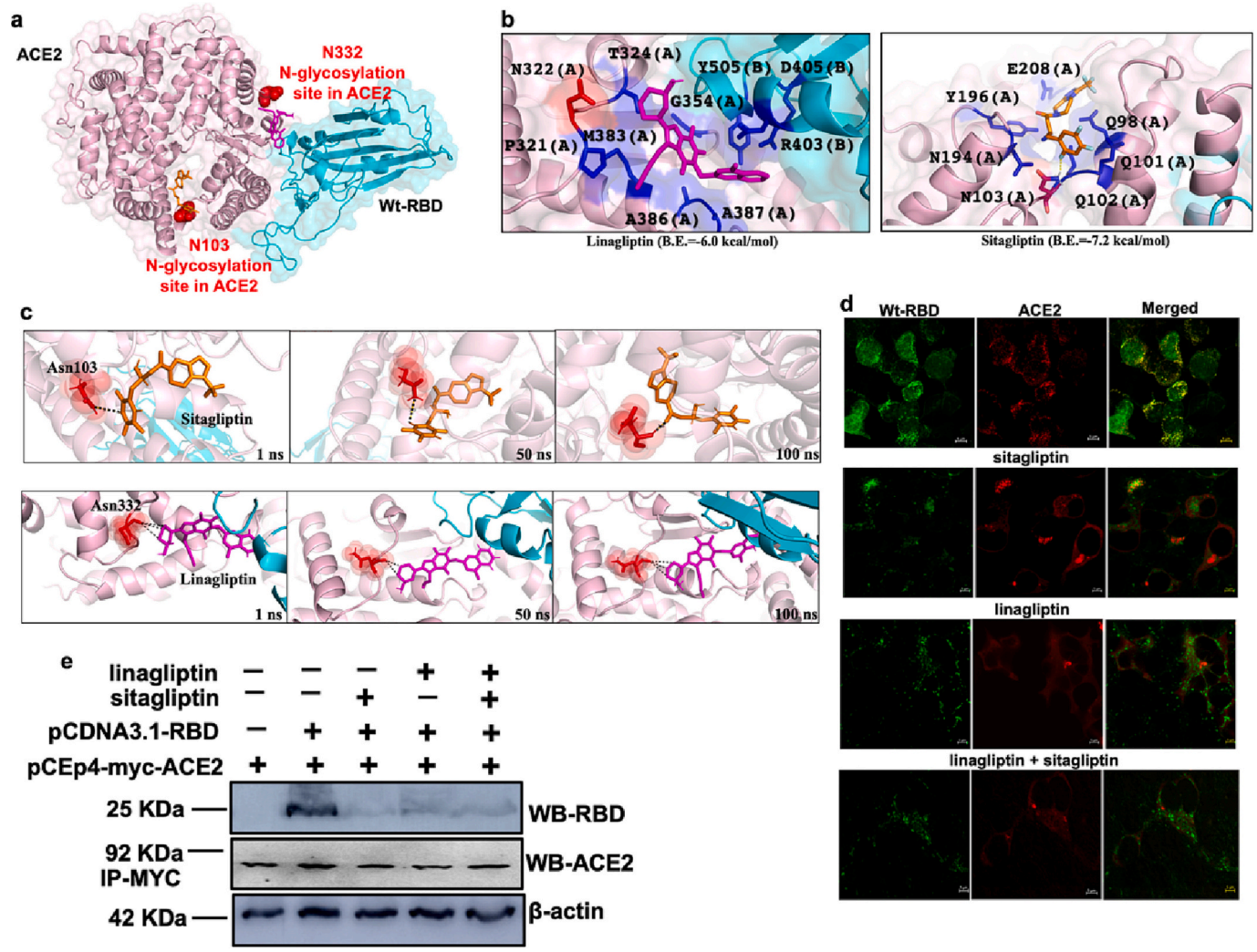

Fig. 5. Binding affinity of RBD with ACE2. a, The best docked pose of sitagliptin (orange) and linagliptin (magenta) with WtRBD-ACE2 complex. The residues N103, and N322 were shown in red sphere. b, The inset depicted interactions of sitagliptin and linagliptin with WtRBD-ACE2 complex residues (blue colour stick). c, Simulations of WtRBD-ACE2 with sitagliptin and linagliptin were illustrated using snapshots of at different timepoints. d, Representative confocal image of RBD-GFP (green) in Calu-3 cells stained with an lexaFluor647-labelled secondary antibody specific to ACE2 (red). Scale bar = 5 μm. e, Calu-3 cells were transfected with myc-tagged ACE2 alone or in combination with pCDNA3.1-RBD in the presence or absence of sitagliptin or linagliptin. All samples were pulled down using myc antibody, and immunoblotted with RBD and ACE2 antibody separately. β-actin was used as an internal control. (For interpretation of the references to colour in this figure legend, the reader is referred to the web version of this article.)

49.7 kDa) appeared as the 49 kDa band (Fig. S6b). The N-terminal His-SUMO-tagged SARS-Cov2 PLpro protein purified through the Ni-NTA column protein is shown in Fig. S6c. N terminus His-SUMO tag of PLpro was cleaved by Ulp1 protease as shown in Fig. S6d. The appearance of two bands corresponding to PLpro and His-SUMO tag and disappearance original uncut protein suggested that the reaction was complete. After removing the His-SUMo tag by Ni-NTA purification (Fig. S6e, left panel), the FPLC purification was done where the PLpro protease peak was observed at 62 ml of elution volume (Fig. 5f). To check the protein purity, the protein was run on SDS PAGE (12 % gel) (Fig. S6e). PLpro tagless protein appeared around 35.6 KDa. This protein with authentic N and C terminus has been used for Gel-based PLpro assay. Similarly, Ulp1 protease and PLpro substrate were induced and confirmed in 12 % SDS-PAGE gel. Induction bands of Ulp1 protease and PLpro substrate were observed at 27.4 KDa and 67 KDa respectively (Fig. S5 g,k). Ulp1 & PLpro protein were purified by Ni-NTA purification column and GST purification column respectively (Fig. S6h,l). Finally, both proteins were purified by the FPLC purification column. The peak for Ulp1 and PLpro substrate were observed at 66.85 ml and 47.5 ml of elution volume during FPLC purification (Fig. S6j,m). PLpro substrate protein eluted in the void volume of the column as dimer (134 kDa) due to the presence of both GST and MBP tags at N and C terminals respectively (Fig. S6m).

3.17. PLpro inhibition assay

Gel-based PLpro assay is a validation assay, as it can wipe out the artefacts which can be seen in the fluorescent-based assay. Thus, we have performed only the gel-based PLpro assay to test whether sitagliptin and linagliptin are as effective as were reported in a few other publications [25,26]. In our study, we were unable to see any significant inhibitory effect of sitagliptin and linagliptin on SARS-CoV-2 PLpro even when tested at high concentration of 500 μM. This contradictory result may be due to the difference in the assay system used. These two compounds have been previously assayed in fluorescence-based assay while we performed gel-based assay. Fluorescence-based assays are highly sensitive and high-throughput in nature, but they occasionally read artefacts, whereas gel-based assays are less sensitive and low-throughput but provide more authentic results, and thus hits filtered in the fluorescence-based assay were validated in Gel-based assay in various

publications. As shown in Fig. 6 a–d (lanes 4–5), in the absence of any inhibitor, PLpro cleaved its substrate into two fragments (25 KDa and 42 KDa) and showed additional two bands along with enzyme (35.6 KDa) and substrate (67 KDa) in SDS-PAGE gel as expected. In the presence of inhibitors, the intensity of cleavage product bands should get reduced and the uncleaved substrate band is expected to get intensified at a significant level. But that is not observed in our experiment in the presence of Sitagliptin and Linagliptin at concentrations of 10 μM, 100 μM, and 500 μM (Fig. 6 a–c). Increasing the pre-incubation time of the enzyme with an inhibitor (from 10 min to 20 min) also produced similar results (Fig. 6d). These negative results were further confirmed by densitometric analysis of all four SDS-PAGE gel images to quantify the relative change of uncleaved substrate band and the cleaved product band (42 KDa) in the presence and the absence of inhibitor. 25 KDa cleaved band was not considered in the present analysis as it was too faint and produced large relative error in calculations. Our analysis suggested no significant inhibitory activity of Sitagliptin and Linagliptin on PLpro activity.

3.18. Main protease (Mpro) inhibition assay

Sitagliptin and linagliptin showed an inhibition of 21.45 ± 0.13 % and 31.46 ± 9.97 % at 100 μM concentration (Fig. 7). However, positive control (Mpro-13b) showed an inhibiton of >80 % at 5uM concentration. It implies that both the gliptins showed minimal effect on Mpro of SARS-CoV-2 inhibition.

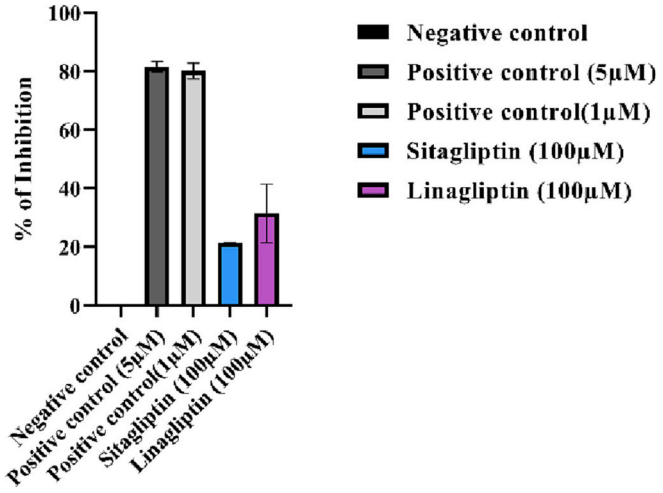

Fig. 7. Inhibition of Mpro enzymatic activity by gliptins. Negative control (no inhibitor), positive control (13b inhibitor) at 5 μM and 1 μM, sitagliptin (100 μM) and linagliptin (100 μM) were tested for Mpro enzymatic activity.

4. Conclusions

By using an experimental and computational approach, we have established that DPP4 is an alternative host receptor for the entry of SARS-CoV-2 into cells. Both cell-surface-binding assay and molecular dynamics simulation study determined that Wt-RBD is interacted with

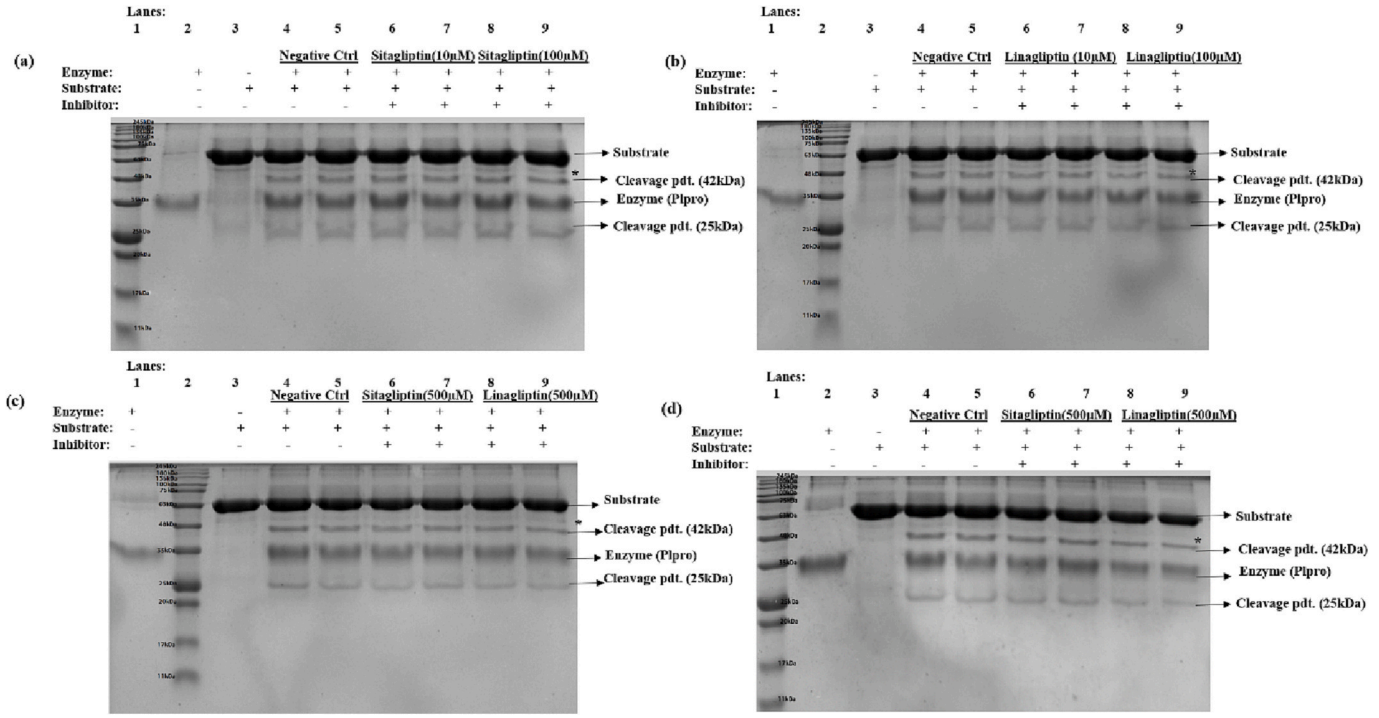

Fig. 6. Gel-based protease assay. (a) lane 1- ladder, lane 2- only enzyme, lane 3- only substrate, lane 4 & 5- Substrate+enzyme, lane 6 & 7- Substrate+enzyme+10 μM Sitagliptin (pre-incubation of enzyme with inhibitor for 10 min before starting the reaction with substrate), lane 8 & 9- Substrate+enzyme+100 μM Sitagliptin (pre-incubation of enzyme with inhibitor for 10 min before starting the reaction with substrate); (b) lane 1- only enzyme, lane 2- ladder, lane 3- only substrate, lane 4 & 5- Substrate+enzyme, lane 6 & 7- Substrate+enzyme+10 μM Linagliptin (pre-incubation of enzyme with inhibitor for 10 min before starting the reaction with substrate), lane 8 & 9- Substrate+enzyme+100 μM Linagliptin (pre-incubation of enzyme with inhibitor for 10 min before starting the reaction with substrate); (c) lane 1- only enzyme, lane 2- ladder, lane 3- only substrate, lane 4 & 5- Substrate+enzyme, lane 6 & 7- Substrate+enzyme+500 μM Sitagliptin (pre-incubation of enzyme with inhibitor for 10 min before starting the reaction with substrate), lane 8 & 9- Substrate+enzyme+500 μM linagliptin (pre-incubation of enzyme with inhibitor for 10 min before starting the reaction with substrate); (d) lane 1- ladder, lane 2- only enzyme, lane 3- only substrate, lane 4 & 5- Substrate+enzyme, lane 6 & 7- Substrate+enzyme+500 μM sitagliptin (pre-incubation of enzyme with inhibitor for 20 min before starting the reaction with substrate), lane 8 & 9- Substrate+enzyme+500 μM linagliptin (pre-incubation of enzyme with inhibitor for 20 min before starting the reaction with substrate). * labelled band is of some impurity which was present along with substrate as it is also evident in lanes having only substrate in it.

DPP4 receptor and binds at the α/β-hydrolase domain of DPP4. Employing a drug repurposing methodology, we have tested gliptins against the SARS-CoV-2 infection. A molecular docking study of the aforementioned gliptins indicated the strong binding affinity of these gliptins with RBD of pan-variants. Among them, sitagliptin and linagliptin, either alone or in combination, have been shown to circumvent the proliferation of pan-VOCs of SARS-CoV-2 infection. Sitagliptin and linagliptin treatment hindered the interaction of RBD with DPP4 at the cell membrane. In this context, a comprehensive and detailed mechanistic study of sitagliptin and linagliptin's inhibitory activity against Wt-RBD-DPP4 complex was conducted using MD simulation. It is found that the two main forces: hydrophobic interaction and hydrogen bonding play a significant role in the strong binding affinity of gliptins with the WtRBD-DPP4 complex. Both sitagliptin and linagliptin were able to inhibit the interaction between Wt-RBD and DPP4 proteins in ACE2 independent manner, which leads to the inhibition of viral growth. Remarkably, it was shown that sitagliptin (IC_{50} value =1.46 μM) and linagliptin (IC_{50} value =2.21 μM), when administered alone or in combination, diminished SARS-CoV-2 infection in all lineages by 6–10 folds at the lowest given concentration. Furthermore, sitagliptin and linagliptin also inhibited the interaction between WtRBD and ACE2, a known cause for SARS-CoV-2 virus entry. The cell-surface binding assay disclosed that the interaction between ACE2 and Wt-RBD was interrupted in the presence of sitagliptin and linagliptin. MD simulation study reveals that sitagliptin and linagliptin were able to block two of the ACE2 receptor's glycosylation sites, N103 and N322, respectively, by interacting with them, which may account for the weak connection between ACE2 and Wt-RBD of SARS-CoV-2. However, the mechanism of glycosylated ACE2 inhibition requires additional wet lab validation, which will be investigated in the future. This data confirms past research that claimed preventing N103 and N322 glycosylation could stop viral entry into the host. In addition, the inhibitory potency of sitagliptin and linagliptin was checked against the enzymatic activity of PLpro and Mpro (responsible for SARS-CoV-2 virus replication) by using in vitro methods. It was discovered that these gliptins had a minimal impact on the inhibition of Mpro and no impact on PLpro inhibition. Overall, sitagliptin and linagliptin alone or in combination are suitable and efficient in preventing all SARS-CoV2 clades since they disrupt the interaction of RBD with both DPP4 and ACE2. Therefore, our discovery confirmed repurposed sitagliptin and linagliptin as a therapeutic strategy has the clinical potential to cure pan-SARS-CoV-2 infections including newly emerging variants.

Supplementary data to this article can be found online at https://doi.org/10.1016/j.ijbiomac.2023.125444.

Declaration of competing interest

Authors declare that they have no competing interests.

Data availability

Data will be made available on request.

Acknowledgements

We acknowledge the Department of Biotechnology Consortium for COVID-19 Research and all the consortium partners for making this study possible. We also thank Dr. Sagar Sengupta, and Dr. Neerja Wadhwa from NII for providing microscopic facility, and valuable inputs. The following reagents were deposited by the Center for Disease control and Prevention, and obtained through BEI resources, NIAID, NIH: SARS-related coronavirus-2, Isolate USA-WA1/2020, NR-52281, Isolate USA/CA_CDC_5574/2020, NR-54011, and Isolate hCoV-19/South Africa/KRISP-K005325/2020, (NR-54009, contributed by Alex Sigal and Tulio de Oliveira). SM is thankful to Translational Research Program-THSTI intramural grant. We thank all staff members of BSL3, THSTI for live virus experiments. We are very grateful to Dr. Debasisa Mohanty, Director, NII for providing full support for computational studies, valuable inputs and guidance. We would like to convey our sincere gratitude Dr. Pramod Garg, Executive director THSTI for his guidance and valuable suggestions. This study was supported by the grants from the CRG-SERB, Govt. of India (CRG/2021/000135) to A.K., and T.M. and by DBT-NII intramural core grant to T.M.

Contributions

S.M., A.K., and T.M. performed all the experiments, formal analysis, investigation, and methodology. Data curation, formal analysis, and reviewing the paper were done by S.M., A.K., K.J., G.K., S.S., A.K., S·K, R.K., and A.K.P. The expression, purification and enzymatic inhibition study of Mpro and PLpro was conducted by S.D., U.P.S. Computational studies, software analysis conceived by A.K., V.B., and T.M. Conceptualization of the project, data curation, formal analysis, funding, investigation, methodology, project validation, writing original draft, review and editing of the manuscript were performed by T.M.

References

[1] J. Lan, J. Ge, J. Yu, S. Shan, H. Zhou, S. Fan, Q. Zhang, X. Shi, Q. Wang, L. Zhang, X. Wang, Structure of the SARS-CoV-2 spike receptor-binding domain bound to the ACE2 receptor, Nature 581 (2020) 215–220, https://doi.org/10.1038/s41586-020-2180-5.

[2] W. Li, M.J. Moore, N. Vasilieva, J. Sui, S.K. Wong, M.A. Berne, M. Somasundaran, J.L. Sullivan, K. Luzuriaga, T.C. Greenough, H. Choe, M. Farzan, Angiotensin-converting enzyme 2 is a functional receptor for the SARS coronavirus, Nature 426 (2003) 450–454, https://doi.org/10.1038/nature02145.

[3] F. Tian, B. Tong, L. Sun, S. Shi, B. Zheng, Z. Wang, X. Dong, P. Zheng, N501Y mutation of spike protein in SARS-CoV-2 strengthens its binding to receptor ACE2, eLife 10 (2021), e69091, https://doi.org/10.7554/eLife.69091.

[4] W. Tai, L. He, X. Zhang, J. Pu, D. Voronin, S. Jiang, Y. Zhou, L. Du, Characterization of the receptor-binding domain (RBD) of, Novel coronavirus: implication for development of RBD protein as a viral attachment inhibitor and vaccine, Cell. Mol. Immunol. 17 (2020) (2019) 613–620, https://doi.org/10.1038/s41423-020-0400-4.

[5] A. Arkhipov, P.L. Freddolino, K. Schulten, Stability and dynamics of virus capsids described by coarse-grained modeling, Structure 14 (2006) 1767–1777, https://doi.org/10.1016/j.str.2006.10.003.

[6] T. Karthika, J. Joseph, V.R.A. Das, N. Nair, P. Charulekha, M.D. Roji, V.S. Raj, SARS-CoV-2 cellular entry is independent of the ACE2 cytoplasmic domain signaling, Cells 10 (2021) 1814, https://doi.org/10.3390/cells10071814.

[7] X.R. Shen, R. Geng, Q. Li, Y. Chen, S.F. Li, Q. Wang, J. Min, Y. Yang, B. Li, R. D. Jiang, X. Wang, X.S. Zheng, Y. Zhu, J.K. Jia, X.L. Yang, M.Q. Liu, Q.C. Gong, Y. L. Zhang, Z.Q. Guan, H.L. Li, Z.H. Zheng, Z.L. Shi, H.L. Zhang, K. Peng, P. Zhou, ACE2-independent infection of T lymphocytes by SARS-CoV-2, Signal Transduct. Target. Ther. 7 (2022) 83, https://doi.org/10.1038/s41392-022-00919-x.

[8] H. Yang, H. Yuan, X. Zhao, M. Xun, S. Guo, N. Wang, B. Liu, H. Wang, Cytoplasmic domain and enzymatic activity of ACE2 are not required for PI4KB dependent endocytosis entry of SARS-CoV-2 into host cells, Virol. Sin. 37 (2022) 380–389, https://doi.org/10.1016/j.virs.2022.03.003.

[9] Z. Song, Y. Xu, L. Bao, L. Zhang, P. Yu, Y. Qu, H. Zhu, W. Zhao, Y. Han, C. Qin, From SARS to MERS, thrusting coronaviruses into the spotlight, Viruses 11 (2019) 59, https://doi.org/10.3390/v11010059.

[10] A. Alnaeem, S. Kasem, I. Qasim, A. Al-Doweriej, M. Refaat, A. Al-Shabebi, M. G. Hemida, The dipeptidyl peptidase-4 expression in some MERS-CoV naturally infected dromedary camels in Saudi Arabia 2018–2019, VirusDisease 31 (2020) 200–203, https://doi.org/10.1007/s13337-020-00586-y.

[11] J. Cui, F. Li, Z.L. Shi, Origin and evolution of pathogenic coronaviruses, Nat. Rev. Microbiol. 17 (2019) 181–192, https://doi.org/10.1038/s41579-018-0118-9.

[12] A. Sebastián-Martín, B.G. Sánchez, J.M. Mora-Rodríguez, A. Bort, I. Díaz-Laviada, Role of dipeptidyl peptidase-4 (DPP4) on COVID-19 physiopathology, Biomedicines 10 (2022) 2026, https://doi.org/10.3390/biomedicines10082026.

[13] R. Strollo, P. Pozzilli, DPP4 inhibition: preventing SARS-CoV-2 infection and/or progression of COVID-19? Diabetes Metab. Res. Rev. 36 (2020), e3330 https://doi.org/10.1002/dmrr.3330.

[14] M.F. Bassendine, S.H. Bridge, G.W. McCaughan, M.D. Gorrell, COVID-19 and comorbidities: a role for dipeptidyl peptidase 4 (DPP4) in disease severity? J. Diabetes 12 (2020) 649–658, https://doi.org/10.1111/1753-0407.13052.

[15] C.F. Chen, C.H. Chien, Y.P. Yang, S.J. Chou, M.L. Wang, T.I. Huo, C.C. Lin, Role of dipeptidyl peptidase-4 inhibitors in patients with diabetes infected with coronavirus-19, J. Chin. Med. Assoc. 83 (2020) 710–711, https://doi.org/10.1097/JCMA.0000000000000338.

[16] S.B. Solerte, A. Di Sabatino, M. Galli, P. Fiorina, Dipeptidyl peptidase-4 (DPP4) inhibition in COVID-19, Acta Diabetol. 57 (2020) 779–783, https://doi.org/10.1007/s00592-020-01539-z.

[17] I. Valencia, Ó. Peiró, C.F. Lorenzo, J. Sánchez-Ferrer, T. Romacho, J. Eckel, DPP4 and ACE2. In diabetes and COVID-19: therapeutic targets for cardiovascular complications? Front. Pharmacol. 11 (2020) 1161, https://doi.org/10.3389/fphar.2020.01161.
[18] C. Klemann, L. Wagner, M. Stephan, S. von Hörsten, Cut to the chase: a review of CD26/dipeptidyl peptidase-4's (DPP4) entanglement in the immune system, Clin. Exp. Immunol. 185 (2016) 1–21, https://doi.org/10.1111/cei.12781.
[19] F. Yang, Y. Dong, B. Li, B. Ning, Q. Zhao, Pancreatic safety of DPP-4 inhibitors in type 2 diabetes millitus: a protocol for systematic review and network meta-analysis, Med. (Baltim.) 101 (2022), e29154, https://doi.org/10.1097/MD.0000000000029154.
[20] M.E. Doyle, J.M. Egan, Mechanisms of action of glucagon-like peptide 1 in the pancreas, Pharmacol. Ther. 113 (2007) 546–593, https://doi.org/10.1016/j.pharmthera.2006.11.007.
[21] C.K.H. Wong, D.T.W. Lui, A.Y.C. Lui, A.C.Y. Kwok, M.C.H. Low, K.T.K. Lau, I.C. H. Au, X. Xiong, M.S.H. Chung, E.H.Y. Lau, B.J. Cowling, Use of DPP4i reduced odds of clinical deterioration and hyperinflammatory syndrome in COVID-19 patients with type 2 diabetes: propensity score analysis of a territory-wide cohort in Hong Kong, Diabetes Metab. 48 (2022), 101307, https://doi.org/10.1016/j.diabet.2021.101307.
[22] B.M. Bonora, A. Avogaro, G.P. Fadini, Disentangling conflicting evidence on DPP-4 inhibitors and outcomes of COVID-19: narrative review and meta-analysis, J. Endocrinol. Investig. 44 (2021) 1379–1386, https://doi.org/10.1007/s40618-021-01515-6.
[23] R. Andreata-Santos, L.M.R. Janini, R. Durães-Carvalho, From alpha to omicron SARS-CoV-2 variants: what their evolutionary signatures can tell us? J. Med. Virol. 94 (2022) 1773–1776, https://doi.org/10.1002/jmv.27555.
[24] P. Mlcochova, S.A. Kemp, M.S. Dhar, G. Papa, B. Meng, I.A.T.M. Ferreira, R. Datir, D.A. Collier, A. Albecka, S. Singh, R. Pandey, J. Brown, J. Zhou, N. Goonawardane, S. Mishra, C. Whittaker, T. Mellan, R. Marwal, M. Datta, S. SenGupta, K. Ponnusamy, V.S. Radhakrishnan, A. Abdullahi, O. Charles, P. Chattopadhyay, P. Devi, D. Caputo, T. Peacock, C. Wattal, N. Goel, A. Satwik, R. Vaishya, M. Agarwal, Indian SARS-CoV-2 Genomics Consortium (INSACOG), Genotype to Phenotype Japan (G2P-Japan) Consortium, , CITIID-NIHR BioResource COVID-19 Collaboration, A. Mavousian, J. Bassi JH, C. Silacci-Fegni, C. Saliba, D. Pinto, T. Irie, I. Yoshida, W.L. Hamilton, K. Sato, S. Bhatt, S. Flaxman, L.C. James, D. Corti, L. Piccoli, W.S. Barclay, P. Rakshit, A. Agrawal, R.K. Gupta, SARS-CoV-2 B.1.617.2 Delta variant replication and immune evasion, Nature 599 (2021) 114–119, https://doi.org/10.1038/s41586-021-03944-y.
[25] A. Narayanan, M. Narwal, S.A. Majowicz, C. Varricchio, S.A. Toner, C. Ballatore, A. Brancale, K.S. Murakami, J. Jose, Identification of SARS-CoV-2 inhibitors targeting Mpro and PLpro using in-cell-protease assay, Commun Biol. 5 (2022) 169, https://doi.org/10.1038/s42003-022-03090-9.
[26] S. Choudhary, S. Nehul, K. A. Kumar, S. Sharma, R. Rani, A. Saha, G. K. Sharma, S. Tomar, P. Kumar, Crystal structure and activity profiling of deubiquitinating inhibitors-bound to SARS-CoV-2 papain like protease revealed new allosteric sites for antiviral therapies. bioRxiv 2022.11.11.516107. doi:https://doi.org/10.1101/2022.11.11.516107.
[27] P. Kumar, R. Pandey, P. Sharma, M.S. Dhar, V.A.B. Uppili, H. Vashisht, S. Wadhwa, N. Tyagi, S. Fatihi, U. Sharma, P. Singh, H. Lall, M. Datta, P. Gupta, N. Saini, A. Tewari, B. Nandi, D. Kumar, S. Bag, D. Gahlot, S. Rathore, N. Jatana, V. Jaiswal, H. Gogia, P. Madan, S. Singh, P. Singh, D. Dash, M. Bala, S. Kabra, S. Singh, M. Mukerji, L. Thukral, M. Faruq, A. Agrawal, P. Rakshit, Integrated genomic view of SARS-CoV-2 in India, Wellcome Open Res. 5 (2020) 184, https://doi.org/10.12688/wellcomeopenres.16119.1.
[28] Y.M. Chong, I.C. Sam, J. Chong, M. Kahar Bador, S. Ponnampalavanar, S.F. Syed Omar, A. Kamarulzaman, V. Munusamy, C.K. Wong, F.H. Jamaluddin, Y.F. Chan, SARS-CoV-2 lineage B.6 was the major contributor to early pandemic transmission in Malaysia, PLoS Negl. Trop. Dis. 14 (2020), e0008744, https://doi.org/10.1371/journal.pntd.0008744.
[29] S. Das, J. Singh, H. Shaman, B. Singh, A. Anantharaj, P. Sharanabasava, R. Pandey, R. Lodha, A.K. Pandey, G.R. Medigeshi, Pre-existing antibody levels negatively correlate with antibody titers after a single dose of BBV152 vaccination, Nat. Commun. 13 (2022) 3451, https://doi.org/10.1038/s41467-022-31170-1.
[30] R. Thiruvengadam, A. Awasthi, G. Medigeshi, S. Bhattacharya, S. Mani, S. Sivasubbu, T. Shrivastava, S. Samal, D. Rathna Murugesan, B. Koundinya Desiraju, P. Kshetrapal, R. Pandey, V. Scaria, P. Kumar Malik, J. Taneja, A. Binayke, T. Vohra, A. Zaheer, D. Rathore, N. Ahmad Khan, H. Shaman, S. Ahmed, R. Kumar, S. Deshpande, C. Subramani, N. Wadhwa, N. Gupta, A. K. Pandey, J. Bhattacharya, A. Agrawal, S. Vrati, S. Bhatnagar, P.K. Garg, Department of Biotechnology India Consortium for COVID-19 research, effectiveness of ChAdOx1 nCoV-19 vaccine against SARS-CoV-2 infection during the Delta (B.1.617.2) variant surge in India: a test-negative, case-control study and a mechanistic study of post-vaccination immune responses, Lancet Infect. Dis. 22 (2022) 473–482, https://doi.org/10.1016/S1473-3099(21)00680-0.
[31] Q. Wang, Y. Zhang, L. Wu, S. Niu, C. Song, Z. Zhang, G. Lu, C. Qiao, Y. Hu, K. Y. Yuen, Q. Wang, H. Zhou, J. Yan, J. Qi, Structural and functional basis of SARS-CoV-2 entry by using human ACE2, Cell 181 (2020) 894–904.e9, https://doi.org/10.1016/j.cell.2020.03.045.
[32] P. Han, C. Su, Y. Zhang, C. Bai, A. Zheng, C. Qiao, Q. Wang, S. Niu, Q. Chen, Y. Zhang, W. Li, H. Liao, J. Li, Z. Zhang, H. Cho, M. Yang, X. Rong, Y. Hu, N. Huang, J. Yan, Q. Wang, X. Zhao, G.F. Gao, J. Qi, Molecular insights into receptor binding of recent emerging SARS-CoV-2 variants, Nat. Commun. 12 (2021) 6103, https://doi.org/10.1038/s41467-021-26401-w.
[33] S. Xu, Y. Wang, Y. Wang, C. Zhang, Q. Hong, C. Gu, R. Xu, T. Wang, Y. Yang, J. Zang, Y. Zhou, Z. Li, Q. Liu, B. Zhou, L. Bai, Y. Zhu, Q. Deng, H. Wang, D. Lavillette, G. Wong, Y. Xie, Y. Cong, Z. Huang, Mapping cross-variant neutralizing sites on the SARS-CoV-2 spike protein, Emerg, Microbes Infect. 11 (2022) 351–367, https://doi.org/10.1080/22221751.2021.2024455.
[34] Y. Wang, C. Liu, C. Zhang, Y. Wang, Q. Hong, S. Xu, Z. Li, Y. Yang, Z. Huang, Y. Cong, Structural basis for SARS-CoV-2 Delta variant recognition of ACE2 receptor and broadly neutralizing antibodies, Nat. Commun. 13 (2022) 871, https://doi.org/10.1038/s41467-022-28528-w.
[35] A. Marco, N. Franko, S.W. Tilles, J. Logue, M.C. Miranda, M. Ahlrichs, L. Carter, G. Snell, M.S. Pizzuto, H.Y. Chu, W.C. Van Voorhis, D. Corti, D. Veesler, Molecular basis of immune evasion by the Delta and kappa SARS-CoV-2 variants, Science 374 (2021) 1621–1626, https://doi.org/10.1126/sciadv.aaw3896.
[36] N. Wang, X. Shi, L. Jiang, S. Zhang, D. Wang, P. Tong, D. Guo, L. Fu, Y. Cui, X. Liu, K.C. Arledge, Y.H. Chen, L. Zhang, X. Wang, Structure of MERS-CoV spike receptor-binding domain complexed with human receptor DPP4, Cell Res. 23 (2013) 986–993, https://doi.org/10.1038/cr.2013.92.
[37] I.T. Desta, K.A. Porter, B. Xia, D. Kozakov, S. Vajda, Performance and its limits in rigid body protein-protein docking, Structure 28 (2020) 1071–1081.e3, https://doi.org/10.1016/j.str.2020.06.006.
[38] W.L. DeLano, The PyMOL Molecular Graphics System, Delano Scientific, 2002.
[39] R.A. Laskowski, M.B. Swindells, LigPlot+: multiple ligand-protein interaction diagrams for drug discovery, J. Chem. Inf. Model. 51 (2011) 2778–2786, https://doi.org/10.1021/ci200227u.
[40] L.C. Xue, J.P. Rodrigues, P.L. Kastritis, A.M. Bonvin, A. Vangone, PRODIGY: a web server for predicting the binding affinity of protein-protein complexes, Bioinformatics 32 (2016) 3676–3678, https://doi.org/10.1093/bioinformatics/btw514.
[41] B. Gallwitz, Clinical use of DPP-4 inhibitors, Front. Endocrinol. 10 (2019) 389, https://doi.org/10.3389/fendo.2019.00389.
[42] R. Pathak, M.B. Bridgeman, Dipeptidyl peptidase-4 (DPP-4) inhibitors in the management of diabetes, P T. 35 (2010) 509–513.
[43] O. Trott, A.J. Olson, AutoDock Vina: improving the speed and accuracy of docking with a new scoring function, efficient optimization, and multithreading, J. Comput. Chem. 31 (2010) 455–461, https://doi.org/10.1002/jcc.21334.
[44] Q. Wang, Y. Zhang, L. Wu, S. Niu, C. Song, Z. Zhang, G. Lu, C. Qiao, Y. Hu, K.-Y. Yuen, Q. Wang, H. Zhou, J. Yan, J. Qi, Structural and functional basis of SARS-CoV-2 entry by using human ACE2, Cell 181 (2020) 894–904, https://doi.org/10.1016/j.cell.2020.03.045.
[45] T. Majumdar, S. Sharma, M. Kumar, Md.A. Hussain, N. Chauhan, I. Kalia, A. K. Sahu, V.S. Rana, R. Bharti, A.K. Haldar, A.P. Singh, S. Mazumder, Tryptophan-kynurenine pathway attenuates β-catenin-dependent pro-parasitic role of STING-TICAM2-IRF3-IDO1 signalosome in *toxoplasma gondii* infection, Cell Death Dis. 10 (2019) 161, https://doi.org/10.1038/s41419-019-1420-9.
[46] M.J. Abraham, T. Murtola, R. Schulz, S. Páll, J.C. Smith, B. Hess, E. Lindahl, GROMACS: high performance molecular simulations through multi-level parallelism from laptops to supercomputers, SoftwareX 1-2 (2015) 19–25, https://doi.org/10.1016/j.softx.2015.06.001.
[47] A.K. Malde, L. Zuo, M. Breeze, M. Stroet, D. Poger, P.C. Nair, C. Oostenbrink, A. E. Mark, An automated force field topology builder (ATB) and repository: version 1.0, J. Chem. Theor. Comput. 7 (2011) 4026–4037, https://doi.org/10.1021/ct200196m.
[48] P. Bjelkmar, P. Larsson, M.A. Cuendet, B. Hess, E. Lindahl, Implementation of the CHARMM force field in GROMACS: analysis of protein stability effects from correction maps, virtual interaction sites, and water models, J. Chem. Theor. Comput. 6 (2010) 459–466, https://doi.org/10.1021/ct900549r.
[49] U. Essmann, L. Perera, M.L. Berkowitz, T. Darden, H. Lee, L.G. Pedersen, A smooth particle mesh Ewald method, J. Chem. Phys. 103 (1995) 8577–8593, https://doi.org/10.1063/1.470117.
[50] M. Parrinello, A. Rahman, Polymorphic transitions in single crystals: a new molecular dynamics method, J. Appl. Phys. 52 (1981) 7182–7190, https://doi.org/10.1063/1.328693.
[51] G. Bussi, D. Donadio, M. Parrinello, Canonical sampling through velocity rescaling, J. Chem. Phys. 126 (2007), 014101, https://doi.org/10.1063/1.2408420.
[52] R. Kumari, R. Kumar, Open-Source Drug Discovery Consortium, A, Lynn, g_Mmpbsa—a GROMACS tool for high-throughput MM-PBSA calculations, J. Chem. Inf. Model. 54 (2014) 1951–1962, https://doi.org/10.1021/ci500020m.
[53] A. Dwivedy, R. Mariadasse, M. Ahmad, S. Chakraborty, D. Kar, S. Tiwari, S. Bhattacharyya, S. Sonar, S. Mani, P. Tailor, T. Majumdar, J. Jeyakanthan, B. K. Biswal, Characterization of the NiRAN domain from RNA-dependent RNA polymerase provides insights into a potential therapeutic target against SARS-CoV-2, PLoS Comput. Biol. 17 (2021), e1009384, https://doi.org/10.1371/journal.pcbi.1009384.
[54] X. Lu, L. Wang, S.K. Sakthivel, B. Whitaker, J. Murray, S. Kamili, B. Lynch, L. Malapati, S.A. Burke, J. Harcourt, A. Tamin, N.J. Thornburg, J.M. Villanueva, S. Lindstrom, US CDC real-time reverse transcription PCR panel for detection of severe acute respiratory syndrome coronavirus 2, Emerg. Infect. Dis. 26 (2020) 1654–1665, https://doi.org/10.3201/eid2608.201246.
[55] C.T. Lim, K.W. Tan, M. Wu, R. Ulferts, L.A. Armstrong, E. Ozono, L.S. Drury, J. C. Milligan, T.U. Zeisner, J. Zeng, F. Weissmann, B. Canal, G. Bineva-Todd, M. Howell, N. O'Reilly, R. Beale, Y. Kulathu, K. Labib, J.F.X. Diffley, Identifying SARS-CoV-2 antiviral compounds by screening for small molecule inhibitors of Nsp3 papain-like protease, Biochem. J. 478 (2021) 2517–2531, https://doi.org/10.1042/BCJ20210244.
[56] F. Guerrero, A. Ciragan, H. Iwai, Tandem SUMO fusion vectors for improving soluble protein expression and purification, Protein Expr. Purif. 116 (2015) 42–49, https://doi.org/10.1016/j.pep.2015.08.019.

[57] S. Iketani, F. Forouhar, H. Liu, S.J. Hong, F.Y. Lin, M.S. Nair, A. Zask, Y. Huang, L. Xing, B.R. Stockwell, A. Chavez, D.D. Ho, Lead compounds for the development of SARS-CoV-2 3CL protease inhibitors, Nat. Commun. 12 (2021) 1–24, https://doi.org/10.1021/acsptsci.0c00108.
[58] L. Zhang, L. Daizong, S. Xinyuanyuan, U. Curth, C. Drosten, L. Sauerhering, S. Becker, K. Rox, R. Hilgenfelld, Crystal structure of SARS-CoV-2 main protease provides a basis for design of improved α-ketoamide inhibitors, Science 368 (2020) 409–412, https://doi.org/10.1126/science.abb3405.
[59] S. Arulmozhiraja, N. Matsuo, E. Ishitsubo, S. Okazaki, H. Shimano, H. Tokiwa, Comparative binding analysis of dipeptidyl peptidase IV (DPP-4) with antidiabetic drugs – an ab initio fragment molecular orbital study, PLoS One 11 (2016), e0166275, https://doi.org/10.1371/journal.pone.0166275.
[60] A.R. Mehdipour, G. Hummer, Dual nature of human ACE2 glycosylation in binding to SARS-CoV-2 spike, Proc. Natl. Acad. Sci. U. S. A. 118 (2021), e2100425118, https://doi.org/10.1073/pnas.2100425118.
[61] Q. Yang, T.A. Hughes, A. Kelkar, X. Yu, K. Cheng, S. Park, W.C. Huang, J.F. Lovell, S. Neelamegham, Inhibition of SARS-CoV-2 viral entry upon blocking N- and O-Glycan elaboration, eLife 9 (2020), e61552, https://doi.org/10.7554/eLife.61552.